Marine and Petroleum Geology 60 (2015) 34–53

Contents lists available at ScienceDirect

Marine and Petroleum Geology

journal homepage: www.elsevier.com/locate/marpetgeo

Research paper

Sandwaves and sand transport on the Barents Sea continental slope offshore northern Norway

Reidulv Bøe [a, *], Jofrid Skarðhamar [b], Leif Rise [a], Margaret F.J. Dolan [a], Valérie K. Bellec [a], Monica Winsborrow [c], Øystein Skagseth [b], Jochen Knies [a], Edward L. King [d], Olav Walderhaug [e], Shyam Chand [a], Stefan Buenz [f], Jürgen Mienert [f]

[a] Geological Survey of Norway (NGU), P.O. Box 6315 Sluppen, 7491 Trondheim, Norway
[b] Institute of Marine Research (IMR), P.O. Box 1870 Nordnes, 5817 Bergen, Norway
[c] Statoil, Harstad, Norway
[d] Geological Survey of Canada-Atlantic (GSC-A), P. O. Box 1006, Dartmouth, Nova Scotia B2Y 4A2, Canada
[e] Statoil, Stavanger, Norway
[f] University of Tromsø (UiT), Department of Geology, 9037 Tromsø, Norway

ARTICLE INFO

Article history:
Received 10 December 2013
Received in revised form
25 May 2014
Accepted 27 October 2014
Available online 4 November 2014

Keywords:
Sandwaves
Sand transport
Continental slope
Time-lapse multibeam bathymetry
Oceanography
Contourite
Tidal current
Internal wave

ABSTRACT

We integrate morphological, geological and geophysical observations with oceanographic measurements and modelling results to interpret the processes behind the origin and evolution of sandwaves on the upper continental slope of the southwestern Barents Sea. Seven sandwave fields covering c. 130 km^2 and with a volume of c. 72 × 10^6 m^3 occur in water depths of c. 475–800 m. Individual sandwaves reach heights up to 6 m. The sandwaves are sinusoidal with asymmetric stoss–lee side relationships, and time lapse multibeam bathymetry analysis indicates that some sandwaves have migrated up to 10 m towards the NNW over a 4-year time period. This contour current parallel migration is counteracted by currents in several other directions, and the sand unit is thus not a simple contourite. Measurements show prominent diurnal period oscillations and clear spring-neap variations of current direction and speed with along-slope and cross-slope current velocities up to 75 cm s^{-1} and 65 cm s^{-1}, respectively. Numerical ocean modelling results produce eddies travelling along the slope, positionally stable, daily recurring vortices and bottom current velocity up to 100 cm s^{-1} in the sandwave fields. Sandwave migration towards the SE is also observed, and the cross-slope currents are capable of transporting sand up and down the slope, as evidenced by ripples migrating normal to the sandwaves. Eroded sand accumulates in the sandwave fields along the boundary between North Atlantic Water and Norwegian Sea Arctic Intermediate Water. This is a consequence of the combined effect of the NNW directed along-slope Norwegian Atlantic Current and tidally induced topographic waves. The sandwave fields started to form 11 000–13 000 ^{14}C yrs BP or possibly later by current erosion of glacial sediments on the continental shelf and slope.

1. Introduction

Sandwaves have been widely documented on continental shelves around the world (e.g., Flemming, 1980; Viana et al., 1998). Their formation requires the operation of bottom currents to erode, transport and deposit sands. Local variations in topography, sediment availability, hydrodynamic regime and global variations in climate and sea-level influence their formation, distribution and evolution. The dynamic nature of sandwaves can present a navigation hazard in shallow areas and pose a risk to seabed infrastructure such as pipelines.

Mud-dominated sediment waves in deepwater environments have been described from many areas and attributed to downslope-flowing turbidity currents and alongslope-flowing bottom (contour) currents (e.g., Wynn and Stow, 2002). Detailed studies of sandwaves in deepwater environments are more limited (Faugéres et al., 1999), but with increasing availability of high resolution marine geophysical and oceanographic datasets, supplemented by modelling, we now have the potential to gain a better understanding of how sandwaves form and evolve. Known occurrences of sandwaves on the continental slope include those in the

* Corresponding author. Tel.: +47 9909 1737.
E-mail address: reidulv.boe@ngu.no (R. Bøe).

http://dx.doi.org/10.1016/j.marpetgeo.2014.10.011
0264-8172/

South China Sea (Reeder et al., 2011), the Strait of Gibraltar (Heezen and Hollister, 1971), Gulf of Cadiz (Kenyon and Belderson, 1973; Baraza et al., 1999; Habgood et al., 2003; Hanquiez et al., 2007), and the Faeroe-Shetland Channel (Kenyon, 1986; Masson, 2001).

The sandwaves on the southwestern Barents Sea continental margin were first noted from sidescan investigations by Kenyon (1986). The sandwaves occur at c. 475–800 m water depth, and are most prolific in two areas (Fig. 1). Video data acquired under the MAREANO programme (www.mareano.no) indicated that they are mainly composed of well-sorted sand transported by the Norwegian Atlantic Current (NAC) towards the NNW. However, sediment transport directions suggested by the orientation of sandwaves and superimposed sand ripples indicated a more complex hydrologic regime than a simple continuous northward contour current which drives the bedforms. Thus, a project under the Norwegian Deepwater Programme (NDP, 2014) was initiated to study the sandwaves. The present paper is the last in a series of three, where the first, by King et al. (2014), presented a detailed description and statistical analyses of the sandwaves based on existing MAREANO data, and the second, by Skarðhamar et al. (in press), oceanographic measurements and modelling results. Here, we integrate geological and morphological observations, including time lapse multibeam bathymetry, with the oceanographic results to interpret the processes behind the origin and evolution of the sandwave fields.

2. Physical setting

2.1. Geological setting

The continental shelf offshore northern Norway has been glaciated multiple times during the Quaternary (Sættem et al., 1992; Vorren et al., 1998), and during the last glaciation it was located at the confluence of the Fennoscandian and Barents Sea ice sheets (Vorren and Kristoffersen, 1986; Landvik et al., 1998; Winsborrow et al., 2010). During maximum glaciation, the ice sheets covered the entire continental shelf, reaching the shelf edge. Major ice streams operated at this time in cross-shelf troughs, including the Bear Island Trough and Håkjerringdjupet (Fig. 1) and discharged large volumes of sediment and meltwater (Vorren and Laberg, 1996; Ottesen et al., 2008; Winsborrow et al., 2010). The glacigenic sequence of the SW Barents Sea has been described as a succession of prograding units with glacial debris flows (e.g., Vorren et al., 1991; Sættem et al., 1992, 1994; Rafaelsen et al., 2002; Andreassen et al., 2004). Stratified units were deposited predominantly in glacial marine environments when the ice margin retreated from the outermost shelf (Rise et al., 2012), and fine-grained sediments accumulated very slowly on the shelf and slope during interglacial periods. Chronological control is limited, however the few available dates suggest that initial ice retreat from the shelf edge occurred prior to c. 14 500 ^{14}C yrs BP (Rüther et al., 2011).

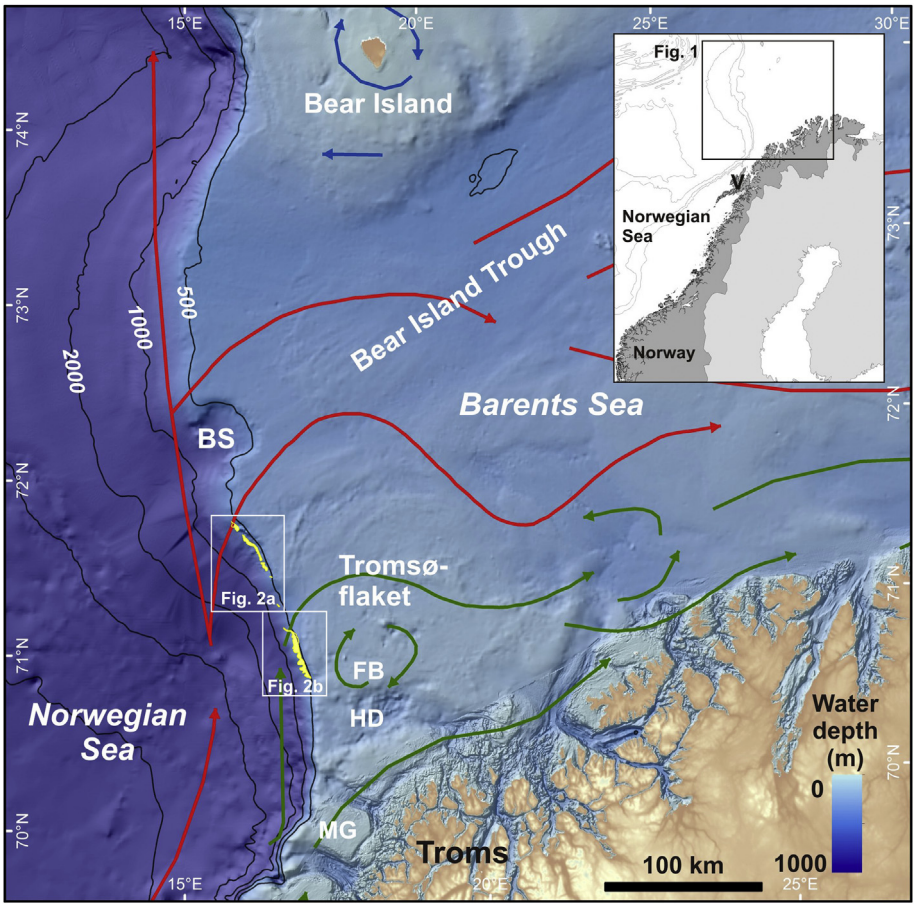

Figure 1. Bathymetric map of the southwestern Barents Sea and continental slope showing the location of the main southern and northern sandwave areas (yellow polygons), surface ocean currents and place names mentioned in the text. Red arrows: Norwegian Atlantic Current; green arrows: Norwegian Coastal Current; blue arrows: arctic water; HD: Håkjerringdjupet; FB: Fugløybanken; BS: Bear Island Slide; V: Vesterålen. (For interpretation of the references to colour in this figure legend, the reader is referred to the web version of this article.)

The south-western Barents Sea continental slope is characterized by multiple buried and seafloor downslope gullies (Kenyon, 1987; Laberg and Vorren, 1995; Laberg et al., 2010). These document glacigenic debris flow and meltwater discharge during glacial periods, as well as slides and mass-movement activity. Sandwave fields, first noted by Kenyon (1986), occur discontinuously along 120 km of the slope in water depths of c. 475–800 m (Figs. 1, 2a, b). The northern sandwave fields (N1–N6; Fig. 2a) are located in a relatively smooth part of the slope with less than 1 m deep, braided and anastomosing chutes indicative of large glacial debris flow activity (King et al., 2014). In contrast, the southern sandwave field (S1; Fig. 2b) is located in a part of the slope which is steeper with more abundant slide scars and gullies that acted as routes for glacial debris flows.

2.2. Bathymetric setting

The sandwave fields are located on the continental slope west of the bank Tromsøflaket (Figs. 1, 2a, b). At the southern end of the southern sandwave field, the inclination of the slope is c. 2.6°; this decreases to c. 1.3° at the northernmost sandwave field. Gullies on the slope west of Tromsøflaket are incised 30–40 m in the sandwave area, deepening lower on the slope. Slide escarpments on the slope exhibit relief of up to 50 m. The continental shelf break occurs at c. 400 m water depth. To the south, the distance between the shelf break and Tromsøflaket is only a few kilometres while this distance increases northwards. Water depths on Tromsøflaket vary from 115 m at its shallowest in the south, to c. 350 m in the north, where there is a gradual transition to the Bear Island Trough. The western margin of Tromsøflaket is topped by N–S-trending long and elevated moraines (Fig. 2b). The relatively flat-lying Bear Island Trough stretches eastwards from the shelf break, in the north, with water depths of 350–500 m. The Bear Island Slide cuts into the shelf with escarpments that are up to 100 m high. The continental slope along this margin dips rather uniformly westward, into the Norwegian Sea.

2.3. Oceanographic setting

The Norwegian Atlantic Current transports water of Atlantic origin northward through the Norwegian Sea (Hopkins, 1991) and splits into two branches near Tromsøflaket (Fig. 1). One branch of the NAC turns east into the Barents Sea while the other continues northwards along the continental slope towards Svalbard (Furevik, 1998, 2001). Three well defined water masses are differentiated along the continental slope (Hansen and Østerhus, 2000; Hopkins, 1991): North Atlantic Water (NAW) is characterized by salinity >35‰, and is typically found on the upper slope shallower than c. 700 m water depths. NAW has temperatures above 6 °C at the mid-Norwegian margin (Haugan et al., 1991) and flows northeastwards along the slope with typical current speeds of 0.2–0.4 m s^{-1} (Heathershaw et al., 1998), but occasionally reaching surface velocities in excess of 1 m s^{-1} west of Lofoten and Vesterålen (Poulain et al., 1996). Norwegian Sea Arctic Intermediate Water (NSAIW) occurs at c. 700–1000 m depth with temperatures between 0.5 °C and −0.5 °C and is characterized by a salinity minimum (Blindheim, 1990). Norwegian Sea Deep Water (NSDW) with temperature below −0.5 °C occurs below c. 1000 m depth (Hansen and Østerhus, 2000). Except for the uppermost waters, the depth of the transition zone between these water layers is, on average, relatively constant throughout the year (Mork and Skagseth, 2010). The continental slope here forms the eastern boundary of the deep-ocean Lofoten Basin which is characterized by large eddy activity (Poulain et al., 1996; Gascard and Mork, 2008).

Topographic waves and amplification of the diurnal tides have been observed and modelled along the slope (Skarðhamar et al., in press). Mooring data from the northern sandwave area show diurnal variations of temperature, salinity and currents, and strong cross-slope current velocity components. Numerical modelling experiments show that tidally induced topographic waves are present throughout the year, generating strong cross-slope currents but varying geographically in terms of periodicity and amplitude. The northern sandwave area experiences diurnal periodicity with amplitudes of about 200 m (and temperature variations of 5–6 °C at the depth of the sandwaves) while the southern field sees semidiurnal periodicity and smaller amplitudes (Skarðhamar et al., in press).

3. Methods

The study area was mapped using multibeam echosounder (Kongsberg Simrad EM 710, 70–100 kHz range) by the Norwegian Mapping Authority and the Norwegian Defence Research Establishment (FFI) in 2008–2009 as part of the Norwegian offshore seabed mapping programme MAREANO (www.mareano.no). Both bathymetry and backscatter data were recorded. The data density was sufficient for gridding at 5 m, allowing detailed analysis of seabed features but no resolution of superimposed bedforms. A few high resolution seismic lines (Kongsberg TOPAS PS 018 parametric sub-bottom profiler, Chirp modus, secondary beam frequency 0.5–6 kHz) with vertical resolution better than 1 m and penetration of 20–30 m in the sand-covered glacial sediments were also acquired. Sampling for biological, environmental and sedimentological studies was performed by grab, boxcorer, epibenthic sledge and beam trawl. Video surveys were performed using IMR's towed video platform CAMPOD (Buhl-Mortensen et al., 2009).

During a cruise with RV G.O. Sars in 2012, 1144 km of additional TOPAS data were collected, along with grab samples at 38 stations and gravity cores at 9 stations. Cruises in 2011–2012 by UiT (two cruises, Simrad EM 3000) and FFI (Simrad EM 710) remapped parts of sandwave fields N2 and S1 (Fig. 2a, b) by multibeam echosounder in order to obtain data for time lapse studies.

Prior to opening the gravity cores, wet bulk density and magnetic susceptibility of the sediments were measured with a Multi Sensor Core Logger (MSCL). The cores were then opened, described, X-rayed and measured for undrained shear strength and water content. Particle size analysis was carried out using a combination of wet sieving and Coulter laser particle counter. LECO SC-444 was used to measure total organic carbon and total carbon content, and from this, calcium carbonate content was calculated. Petrographic analysis was performed on 14 thin sections of sand from the sandwave fields (Bøe et al., 2013). Visible shell fragments and foraminifera were picked for AMS ^{14}C dating at the ^{14}C CHRONO Centre, Queens University, Belfast.

The oceanographic part of the project included a field campaign to collect data on hydrography and currents in March–April 2012, and numerical model simulations of ocean dynamics. Three current meter moorings were deployed in the sandwave area, and on the recovery cruise, the shelf and slope were surveyed with 11 CTD stations (Fig. 2a). Details of the oceanographic measuring program and the results are presented in Skarðhamar et al. (in press). A moored current meter was also deployed within the northern sandwave area (71°38.81′N, 16°10.99′E) in the period 18 September–20 December 2010 (Fig. 2a). This mooring was equipped with a Nortek 190 kHz current meter at depth 508 m, 100 m above the seabed.

For numerical model simulations of bottom currents, an extended version of the 800 m grid model NorKyst800 was used (Albretsen et al., 2011). This is based on the public domain Regional

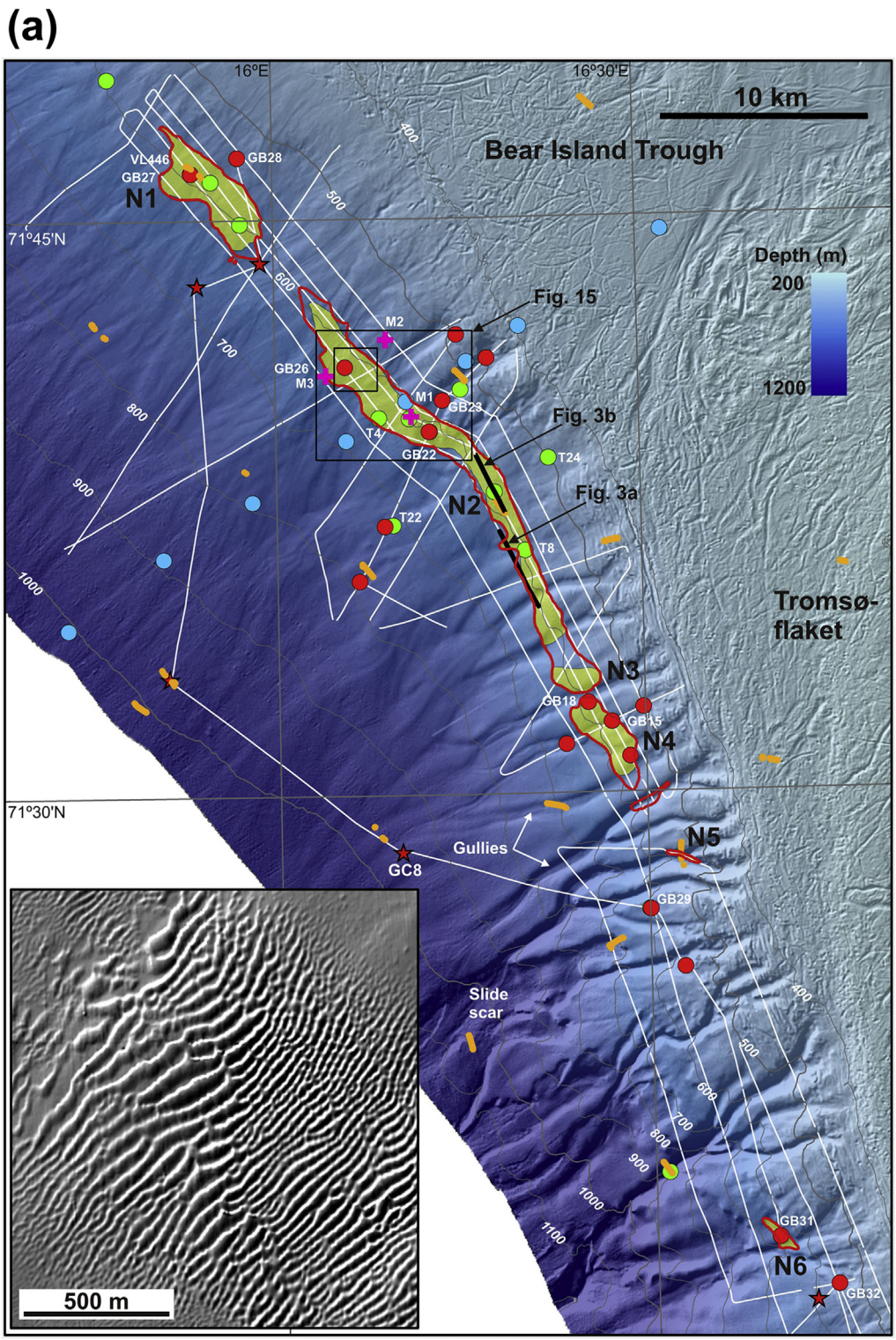

Figure 2. a. Shaded relief bathymetry map from the northern sandwave area showing location of sandwave fields N1–N6 interpreted from MAREANO multibeam data (yellow polygons) and TOPAS data (red outline). TOPAS profiles (white lines), grab samples (GB, red dots), gravity cores (GC, red stars), time series modelling stations (T, green dots), CTD stations (blue dots), mooring stations (M, pink crosses), MAREANO video lines (VL, orange dots), seismic figure examples, and FFI multibeam bathymetry coverage (large black rectangle) are also shown. Small black rectangle shows location of inset enlarged detail from the FFI dataset (shaded relief image illuminated from the NW). Stations mentioned in the text are labelled. See Figure 1 for location. b. Shaded relief bathymetry map from the southern sandwave area showing location of sandwave field S1 interpreted from MAREANO multibeam data (yellow polygons) and TOPAS data (red outline). TOPAS profiles (white lines), grab samples (GB, red dots), gravity cores (GC, red stars), time series modelling stations (T, green dots), MAREANO video lines (VL, orange dots), moraines (M) and FFI multibeam bathymetry coverage (large black rectangle) are also shown. Small black rectangle shows location of inset enlarged detail from the FFI dataset (shaded relief image illuminated from the NW). Stations mentioned in the text are labelled. See Figure 1 for location. (For interpretation of the references to colour in this figure legend, the reader is referred to the web version of this article.)

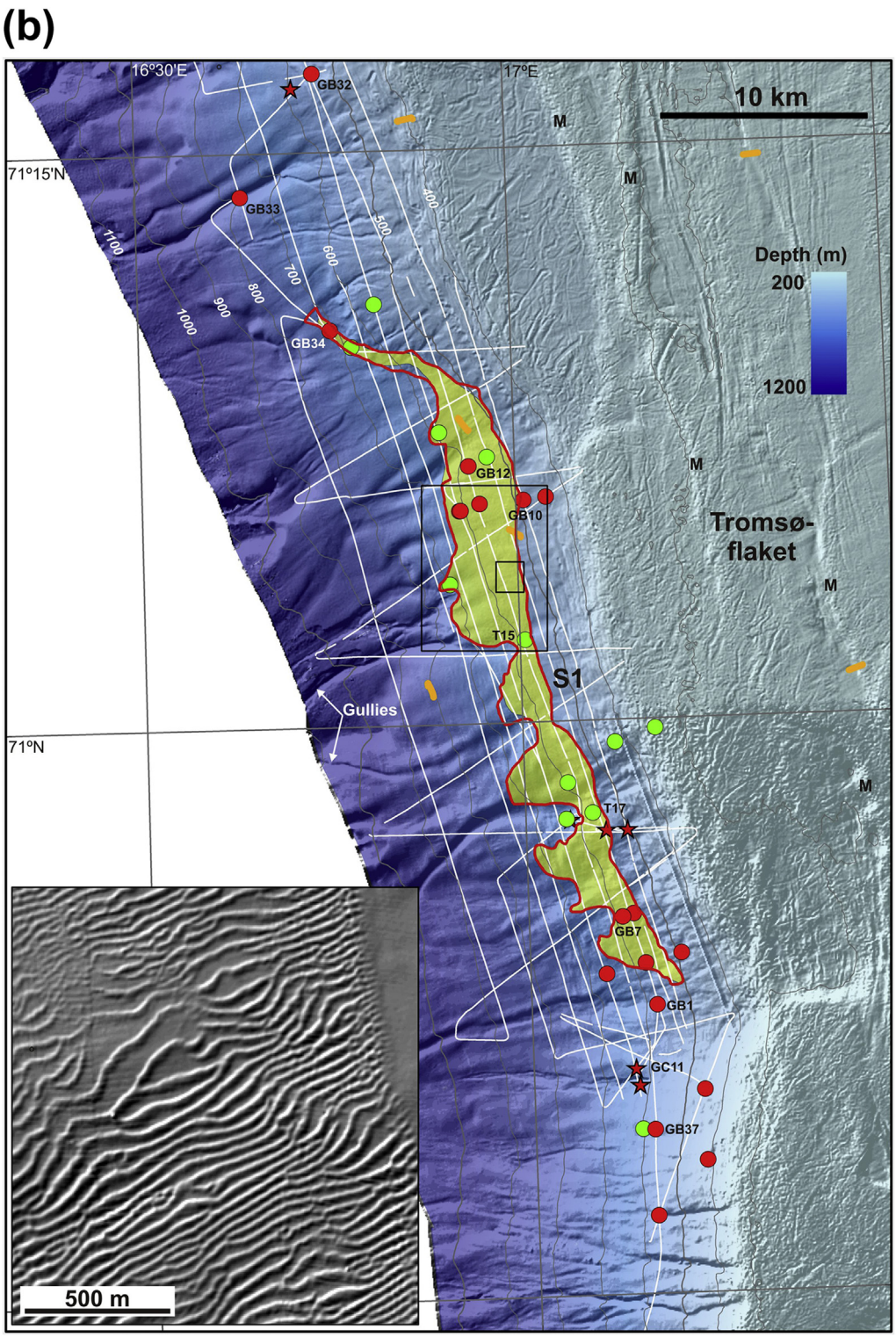

Figure 2. (*Continued*)

Ocean Modelling System (ROMS), version 3 (Haidvogel et al., 2008; Shchepetkin and McWilliams, 2005). The model domain consisted of 680 × 610 grid cells of size 800 m x 800 m horizontally and 35 terrain-following levels vertically. In our model setup the thickness of the deepest model layer was reduced to 7 m in the sandwave area to provide better resolution of the bottom currents than the standard setup. The bathymetric information applied in ROMS was smoothed to avoid model instability and/or spurious deep currents, thus the chutes and gullies intersecting the slope are not resolved in the NorKyst800 bathymetry. The model was forced with lateral boundary conditions from the archive of MET's Nordic 4 km simulation (MET, 2014), river runoff data from the Norwegian Water Resources and Energy Directorate (NVE) (Beldring et al., 2003), atmospheric forcing from ERA-interim (2014), and tides

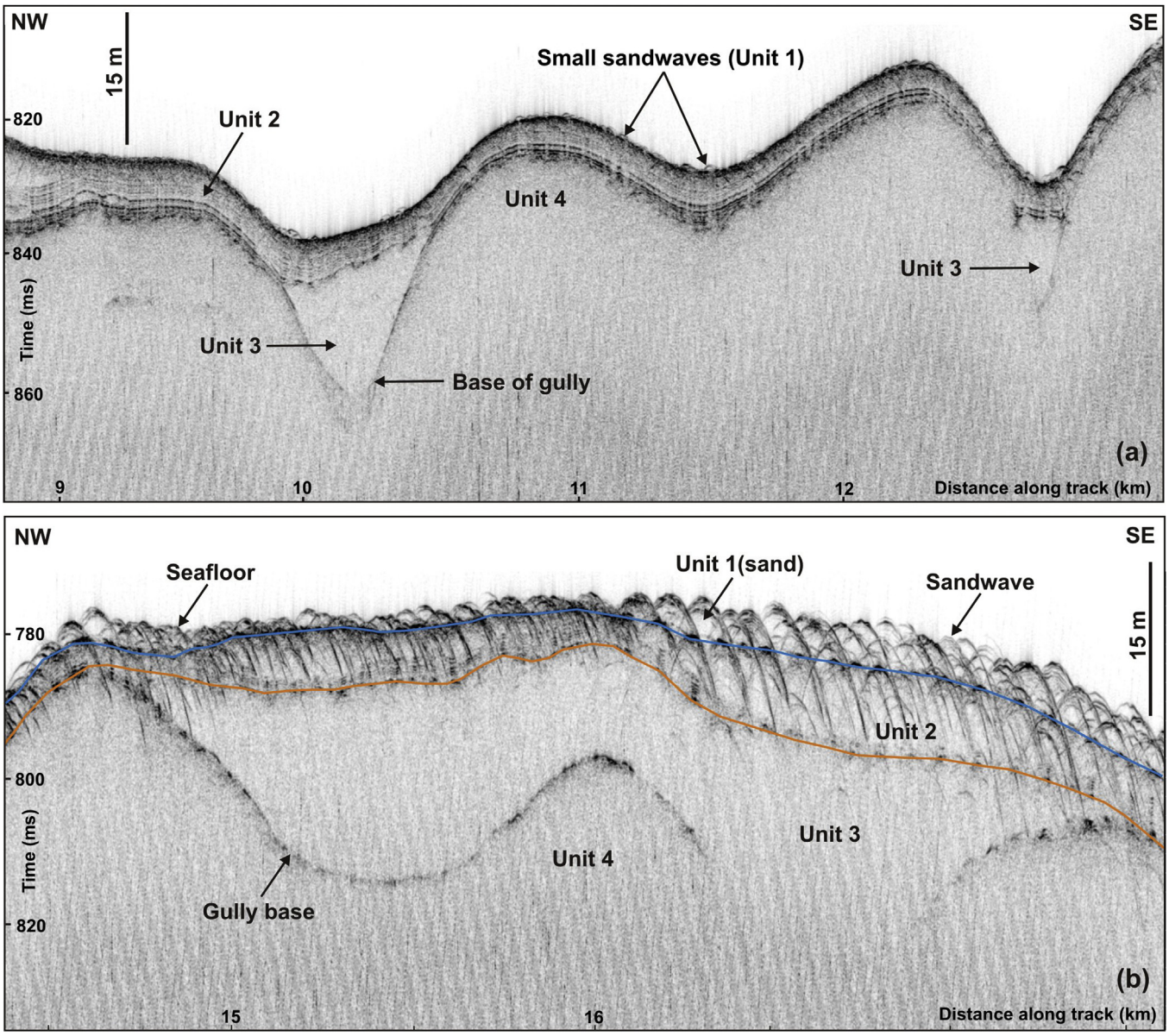

Figure 3. a) TOPAS line along the southernmost part of sandwave field N2 showing small sandwaves (Unit 1), layered glaciomarine sediments (Unit 2) and gullies partly filled by massive, glacial debris flow deposits of Unit 3. b) TOPAS line along the central part of sandwave field N2. Note the numerous hyperbolae created by the sandwaves. Blue line: interpreted base of Unit 1; orange line: interpreted base of Unit 2. See Figure 2a for location of profiles and main text for interpretation. (For interpretation of the references to colour in this figure legend, the reader is referred to the web version of this article.)

based on a global inverse barotropic model of ocean tides (TPXO7.2), including eight primary harmonic constituents (M_2, S_2, N_2, K_1, K_2, O_1, P_1, Q_1) of diurnal frequencies, two long period (Mf, Mm) and three nonlinear (M4, MS4, MN4) constituents. For details about the forcing and model set up see Skarðhamar et al. (in press) and Albretsen et al. (2011).

4. Stratigraphy

4.1. Seismic stratigraphy and distribution of units

Three seismic units recognized in the TOPAS data are exposed on the seabed along the sandwave fields. The uppermost Unit 1 has an acoustic signature indicative of sandwaves. It occurs discontinuously along 120 km of the Barents Sea continental slope in seven sandwave fields in water depths of c. 475–800 m (Fig. 2a, b). The sand unit is present both in gullies and on ridges between gullies as well as into slide scars, and reaches a maximum thickness of c. 6 m (Fig. 3). In many of the sandwave fields, the base of the sandwave unit is easily identified as a strong reflection. In other areas the base of the sandwaves is more diffuse due to side-echoes from the sandwaves.

Gravity cores and grab samples obtained between the sandwave fields, where Unit 1 is absent, show that the seabed is covered by gravelly lag deposits 0–10 cm thick and that the top of Unit 2 has been eroded. Unit 2 is characterized by continuous, parallel reflections of low to medium amplitude. It occurs in the southern part of the study area where it locally reaches a thickness of almost 10 m, while it thins and disappears in a northerly direction. Unit 2 drapes the surface of units 3 and 4. The base of Unit 2 has high-medium reflection amplitude.

Unit 3 is acoustically massive and occurs as up to 50 m thick gully fill above a high-reflectivity erosion surface (Fig. 3). Weak,

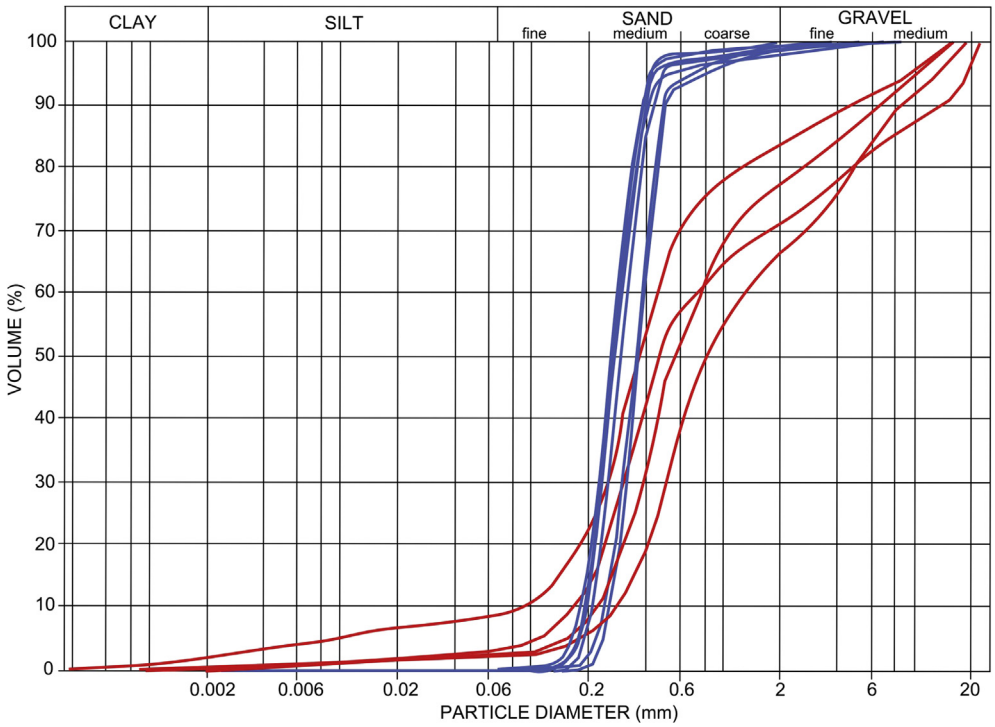

Figure 4. Grain-size distribution curves for grab samples within (blue curves) and outside (red curves) the sandwave fields. See Figure 2a and b for location of the grab samples. (For interpretation of the references to colour in this figure legend, the reader is referred to the web version of this article.)

undulating, concave or convex, semi-continuous reflections are observed within it. It locally occurs on elevated ridges between gullies, but there it is difficult to differentiate between units 3 and 4. Unit 4 is also acoustically massive but has higher amplitudes than Unit 3. The TOPAS data reveal strata similar to Units 2–4 also at deeper levels. Massive units with undulating, concave and convex internal reflectors alternate with thinner, stratified units that are partly or completely removed by erosion.

4.2. Sediment types and radiocarbon dating results

Sand samples were obtained with grab (14 samples) from all the sandwave fields. All samples contain very uniform, medium-grained sand, classified as well sorted according to Folk and Ward (1957). Three grab samples outside of the sandwave fields, between N4 and S1 (Fig. 2a and b), show the same type of well-sorted sand. Two samples from slightly shallower water east of N1 and N2 have a well sorted medium-grained sand fraction but somewhat higher content of coarse sand and gravel. The majority of the samples taken outside of the sandwave fields comprise poorly sorted, gravelly sand, sometimes with 10–20% silt. Of the grain size fractions, it appears that the medium sand is best sorted. None of the grabs in the sandwave fields penetrated through the sand unit. Twelve of the grabs outside the sandwave fields penetrated a gravelly sandy top layer and into mud/clay below. The thickness of the top layer is usually 5–10 cm although it varies from 1 cm to more than 15 cm.

Gravity cores up to 3 m long were obtained to describe the stratigraphic unit(s) below Unit 1. Because gravity corers have difficulties penetrating well sorted sand of more than c. 15 cm, coring locations were placed outside/between sandwave fields where Unit 1 is thin (Fig. 2a, b). Most of the cores comprise normally consolidated clay with scattered gravel indicating that the sediments are mainly of glaciomarine origin (Unit 2). The water content is generally 40–55%, while undrained shear strength (s_u) is in the range 4–10 kPa. Most of the samples show a normal consolidation trend, i.e. decreasing water content and increasing s_u downwards. Some undrained shear strength measurements fall in the range 15–20 kPa. We are uncertain if some cores penetrated into the massive glacial deposits (Units 3 or 4).

Mixed planktic and benthic foraminifera and bivalves from the top of Unit 2 (17–35 cm below the top of GC 8) yield an age range of 12 567–13 007 ± 65 ^{14}C yr BP (using a 440 year marine reservoir correction; Mangerud and Gulliksen, 1975). Located in c. 940 m water depth, downslope of the sandwaves, the core has sandy, gravelly lag in the uppermost few centimetres (Fig. 2a).

5. Description of the sandwave unit (Unit 1)

5.1. Sand distribution and thickness

The extent and thickness of Unit 1 has been mapped by means of multibeam, TOPAS, grab and gravity corer. The TOPAS data reveal smaller sandwaves than the MAREANO multibeam data, while the new FFI multibeam data exhibit the best resolution in two small areas of time lapse multibeam data (see below). Figure 2a and b shows the areal distribution of the sandwave fields of Unit 1. There is no clear trend in sand thickness versus water depth or distance along the continental slope. A slight tendency for increasing sand thickness within downslope gullies is observed, in particular in S1. There are however, gullies where sand thickness is low (e.g., the southern part of N2) and shoulders between gullies with thick sand (e.g., the northern part of N2). King et al. (2014) calculated the total area of the sandwave fields to be 130 km^2 and the total volume of sand, based on sandwave half-height measurements from the MAREANO multibeam bathymetry, to amount to 72 × 10^6 m^3. From the new sub-bottom profiler and multibeam swath bathymetry data it is evident that these numbers can be regarded as minimum values.

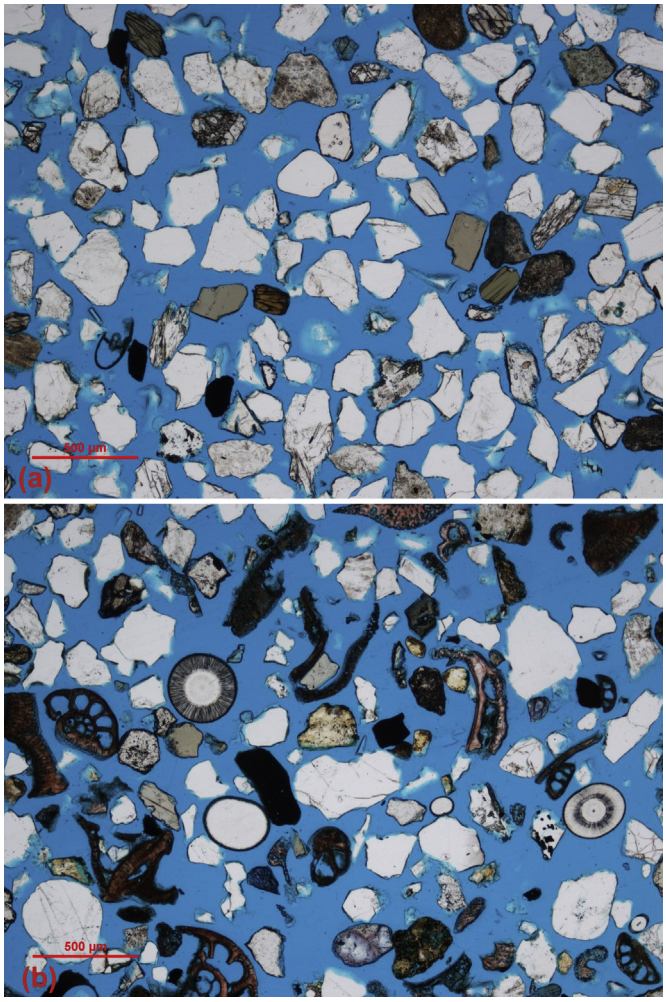

Figure 5. a) Quartz-rich sand, GB12 from the northern part of sandwave field S1. b) Quartz-rich sand with high content of shells (mainly foraminifers and sponge spicules), GB1 from south of sandwave field S1. Plane polarized light. See Figure 2b for location of the grab samples.

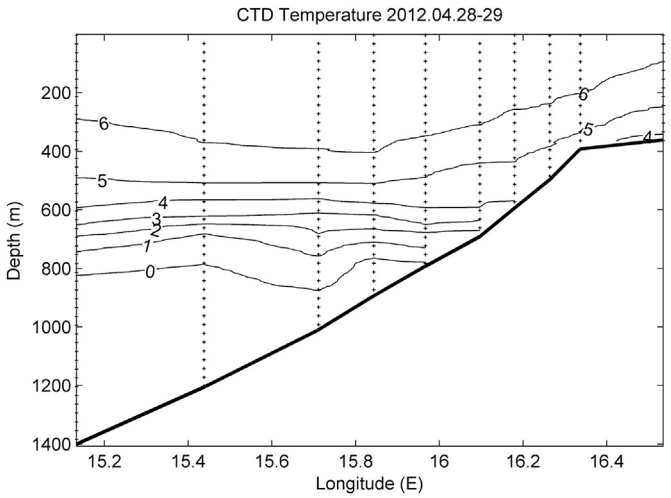

Figure 7. CTD measurements showing temperature (°C) distribution across the shelf and slope west of Tromsøflaket. The current meter mooring was positioned in the northern sandwave field at approximately 16.2°E. The dotted vertical lines denote CTD stations shown in Figure 2a while the *x*-scale refers to longitude. Modified from Skarðhamar et al. (in press).

5.2. Grain-size analyses

Grain size distribution (0–2 cm depth) was analysed from grab samples and top layers in gravity cores. Details of the methods and calculations are given in Bøe et al. (2013). The results show that in S1, the sand is well sorted with almost 100% of the material in the sand fraction and with the majority of the grains in the medium sand fraction (Fig. 4). Sand outside the sandwave field is less well-sorted with more coarse sand and gravel. The best sorting occurs in medium-grained sand.

GB 31 from N6 has a grain-size distribution similar to the other sandwave samples but contains more silt (~4%). Three other samples outside of the sandwave fields (GB 29, GB 32 and GB 33; see Fig. 2a and b for location) have grain-size distribution similar to the sandwave samples. The northernmost samples (GB 22, GB 26 and GB 27; Fig. 2a) are slightly more fine-grained than the samples further south. Outside of the northern sandwave fields,

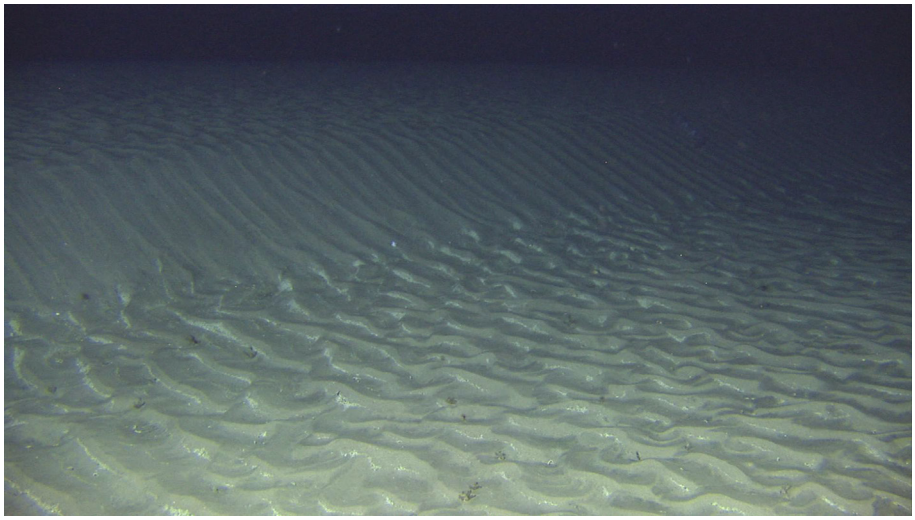

Figure 6. Example of a sandwave within sandwave field N1. Note sand ripples on the lee side of the large sandwave migrating at almost 90° to the crest of the sandwave. See Figure 2a for location.

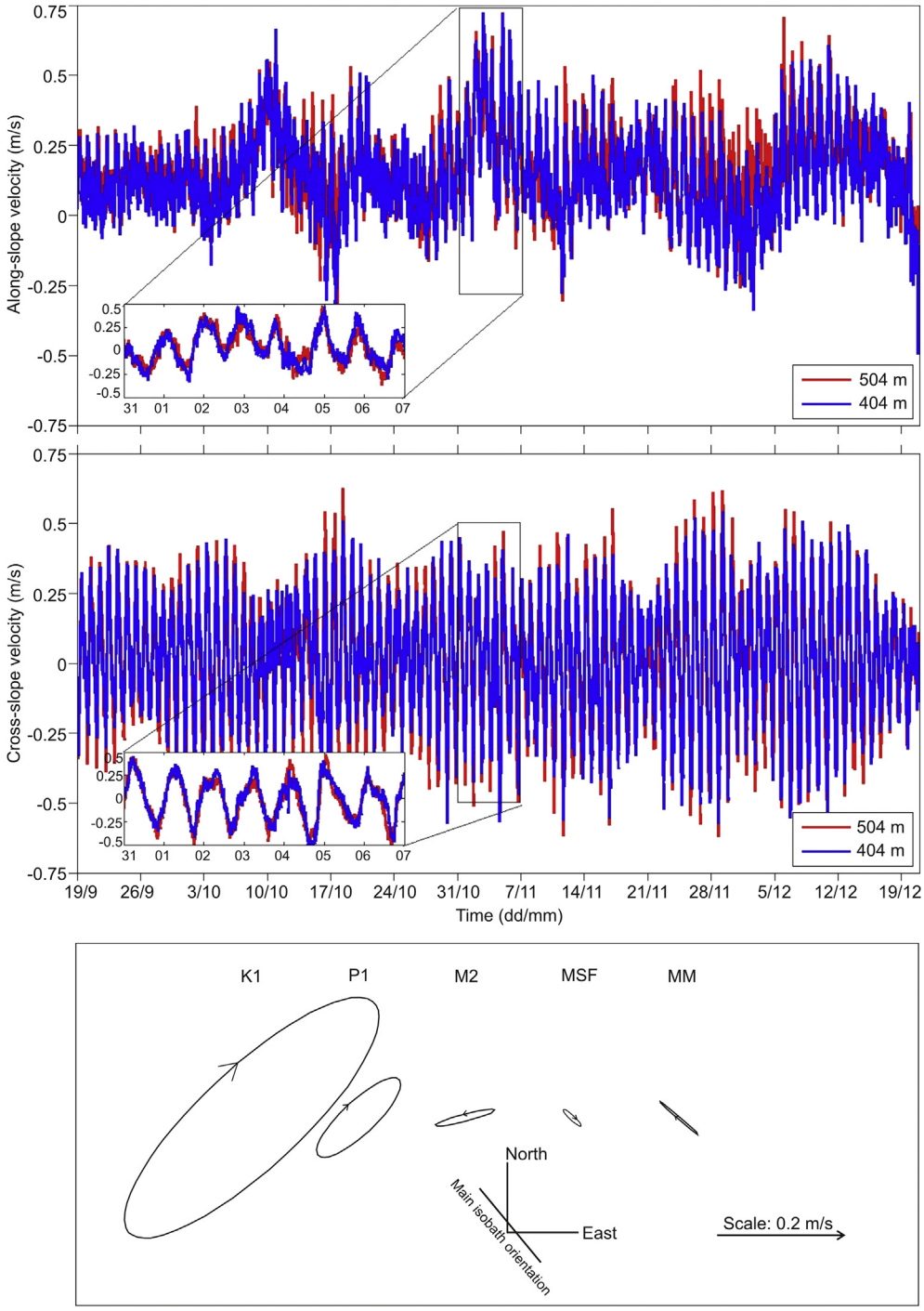

Figure 8. Current measurements from water depths 404 and 504 m in September–December 2010: along-slope (upper panel; positive values towards 320°) and cross-slope (middle panel, positive values towards 50°) current velocity components. Lower panel: Major diurnal (K1, P1), semi-diurnal (M2), and long-periodic (MSF, MM) tidal constituents are shown as tidal ellipses including direction of the rotation. For reference, directions and major orientation of isobaths are shown. Note that the diurnal periods (K1 and P1) clearly dominate with the major axes of variability in cross-shelf (isobath) direction. The mooring was located on water depth 603 m southwest of mooring M1. See Figure 2a for location.

large variations in grain size occur. Samples GB 28 and GB 23 (upslope of N1 and N2) have grain-size distribution similar to the samples within the fields, but somewhat higher coarse sand/fine gravel content.

Median and mean grain size are greatest in the southern part of S1, whereas the smallest grain sizes occur in the northern fields N2 and N1. Sorting (Folk and Ward, 1957) of the main fraction varies very little, but this parameter indicates slightly better sorting in N4 and N2. The sample from N5 shows the poorest sorting in the main fraction. The data show no correlation (there are too few samples for statistical comparison) between mean grain size, sorting and sandwave areas.

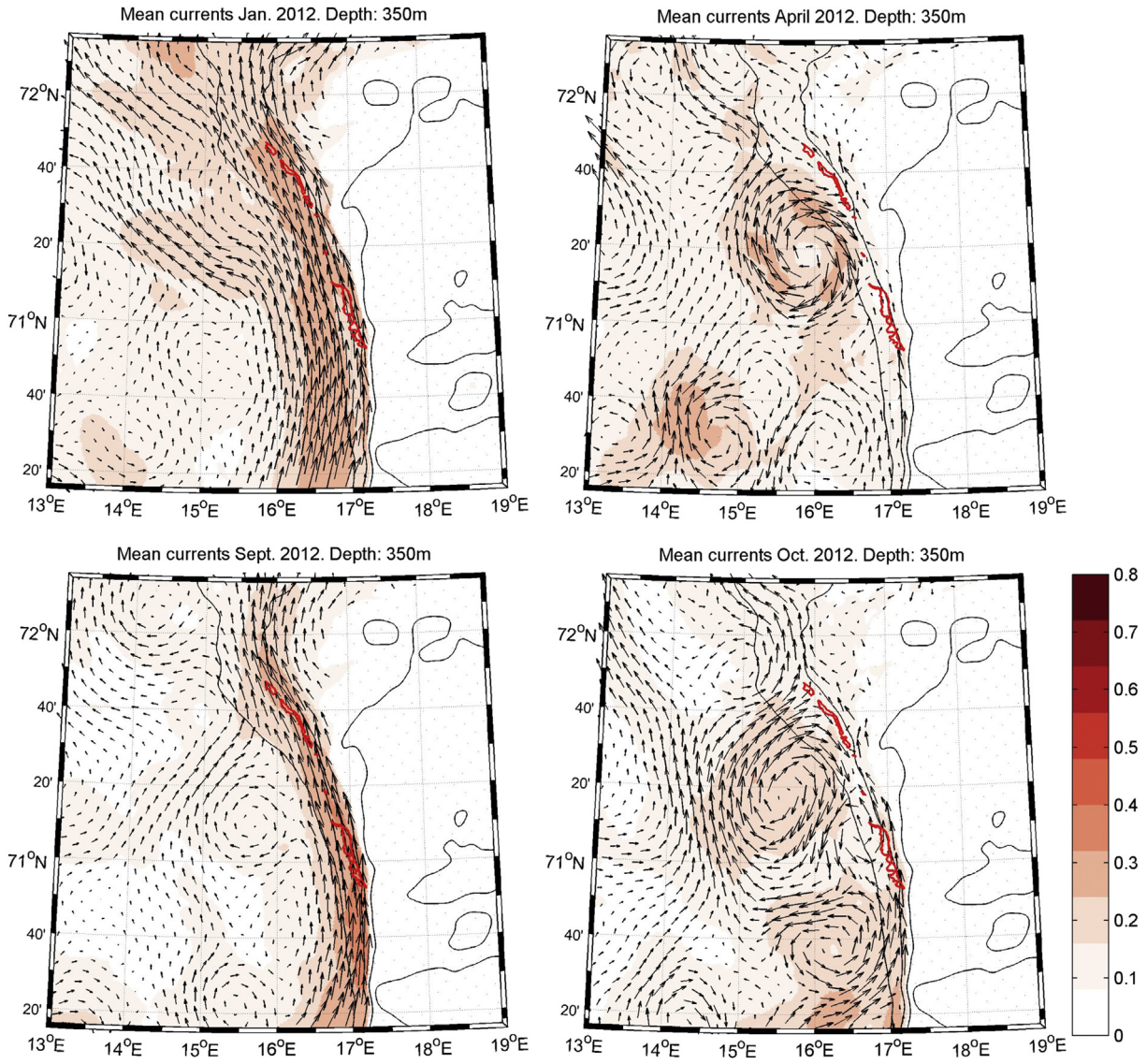

Figure 9. Modelled mean current speed (colour scale, m s^{-1}) and velocity vectors for January, April, September and October 2012 for depths 350 m. Bathymetric contours for depths 200, 300, 500 and 1000 m are indicated with black lines, and the sandwave fields with red contours. Modified from Skarðhamar et al. (in press). (For interpretation of the references to colour in this figure legend, the reader is referred to the web version of this article.)

5.3. Sand composition

Thin sections (Fig. 5) were made of 12 sand samples from the sandwave fields. Prior to thin sectioning, the sand was mounted in stained epoxy. Petrographic analysis of the samples was performed by counting 200 points (excluding porosity) on each thin section (Bøe et al., 2013). The grain size of the sand was determined by measuring the longest cross section of 30 grains per sample. The sand samples do not contain clay or sand-sized mica grains. Glauconitic clay matrix occurs only in porous particles, mainly in carbonate fossils. Also under the microscope it was found that the average grain size is medium sand, and the sorting is generally very good although in some samples there are outsized grains that reduce the degree of sorting.

The dominating sand mineral is quartz (57–68%), but K-feldspar and plagioclase are also common. Some quartz grains have inherited quartz overgrowth. There is a wide range of bedrock fragments, including sandstone, metasandstone, siltstone, gneiss, granite, mica schist, dolomite, chert etc. Heavy minerals are common to abundant and account for 2–19% of the sand. The heavy mineral association is dominated by amphibole and garnet, but clinozoisite and epidote are common. A few grains of numerous other minerals are also present.

Samples from the sandwaves contain up to 5% carbonate shells while the samples from south of S1 contain up to 15% shell material, including siliceous sponge spicules. Total organic carbon (TOC) and total carbon (TC) content were measured on the surface samples that were analysed for grain size. We assumed that all inorganic carbon (excluding some dolomite grains) is bound as $CaCO_3$ (minerals, rock fragments and shell material) and calculated weight percentage in the samples. The geochemical analyses confirm a $CaCO_3$ content of the sandwave sand of up to 5% (mean 1.4%) while samples from outside of the sandwave fields contain up to 42% (mean 13.2%) $CaCO_3$.

MAREANO videos show shell hash in the lee of some sandwaves (King et al., 2014). Visual inspection of the grab samples shows that samples from the sandwaves tend to have the highest carbonate content (mostly shell fragments) in the fraction >1 mm. Samples

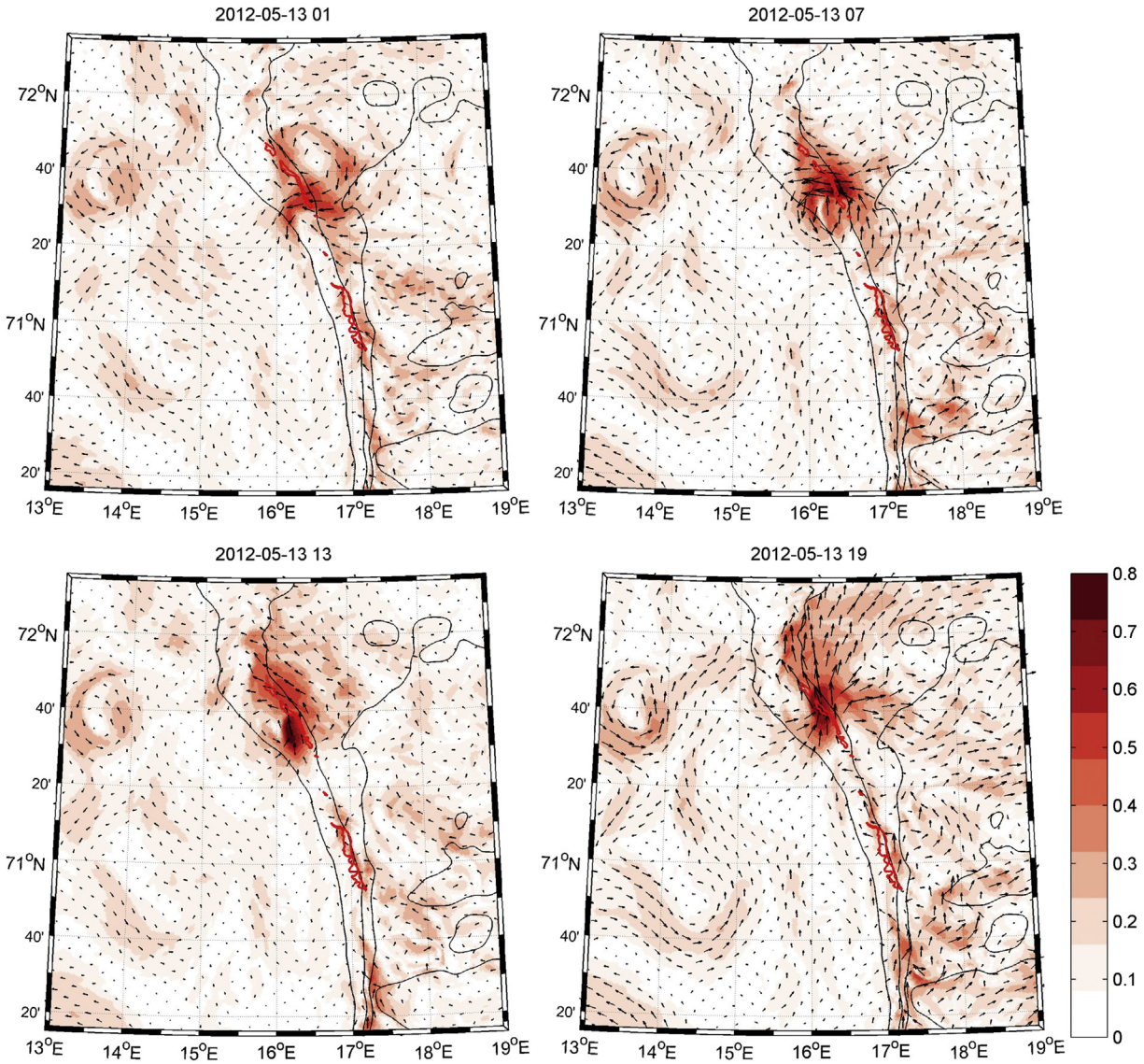

Figure 10. Modelled bottom current speed (colour scale, m s^{-1}) and velocity vectors, time development of instantaneous fields May 13th. Bathymetric contours for depths 200, 300, 500 and 1000 m are indicated with black lines, and the sandwave fields with red contours. Note the eddy appearing at 71°45′N, 16°20′E and its changing direction of rotation. Modified from Skarðhamar et al. (in press). (For interpretation of the references to colour in this figure legend, the reader is referred to the web version of this article.)

outside of the sandwave fields have the highest $CaCO_3$ content (again mostly shell fragments) in the 0.5–1 mm fraction.

5.4. Sandwave morphology

The sandwaves are generally 2-dimensional with occasional bifurcations, and they decrease in size towards the sandwave field boundaries (Figs. 2a, b, 3a). Following the terminology of Belderson et al. (1982) we use the term sandwave to refer to the subaqueous, lower flow regime, transverse bedforms of sand that have larger wave lengths than sand ripples (see also Bøe et al., 2009). Where two or more sizes of sandwaves occur together or superimposed it is convenient to refer to them as small sandwaves (same as dunes or megaripples) and large sandwaves, without implying any genetic difference. This is because there appears to be a complete gradation in size, plan view and lee slope angle between sandwaves at various locations (Belderson et al., 1982).

Sandwave crestlines have a strong SW–NE trend, normal to the bathymetric contours, and the sandwaves are frequently sinusoidal with asymmetrical stoss–lee relationships. They are usually sharp crested with lee sides towards the northwest although individual sandwaves and domains of sandwaves exhibit lee sides towards the southeast. NW slopes are on average marginally steeper than SE slopes. The largest sandwaves occur in sandwave fields N2 and S1. Domains of the larger examples fall along the central axis of the sandwave fields but they are also affected by gullies and slide scars. Sandwave heights show a normal distribution with mean height 0.6 m and maximum height 5–6 m. Wavelengths are on average 64 m with maximum 205 m. A detailed description of the sandwaves is given by King et al. (2014).

A variety of small ripples is superimposed on the sandwaves. The sandwave crest and stoss generally have complex 3-D ripples (generally linguoid) with current sense normal to the crestline (Bøe et al., 2013). A remarkable change in ripple type and orientation occurs at the crest of sandwaves, with 2-D ripples with linear crests and occasional bifurcations occurring at their lee sides (Fig. 6). They are asymmetric and have crest orientations highly oblique to the sandwave crestline, occasionally almost normal.

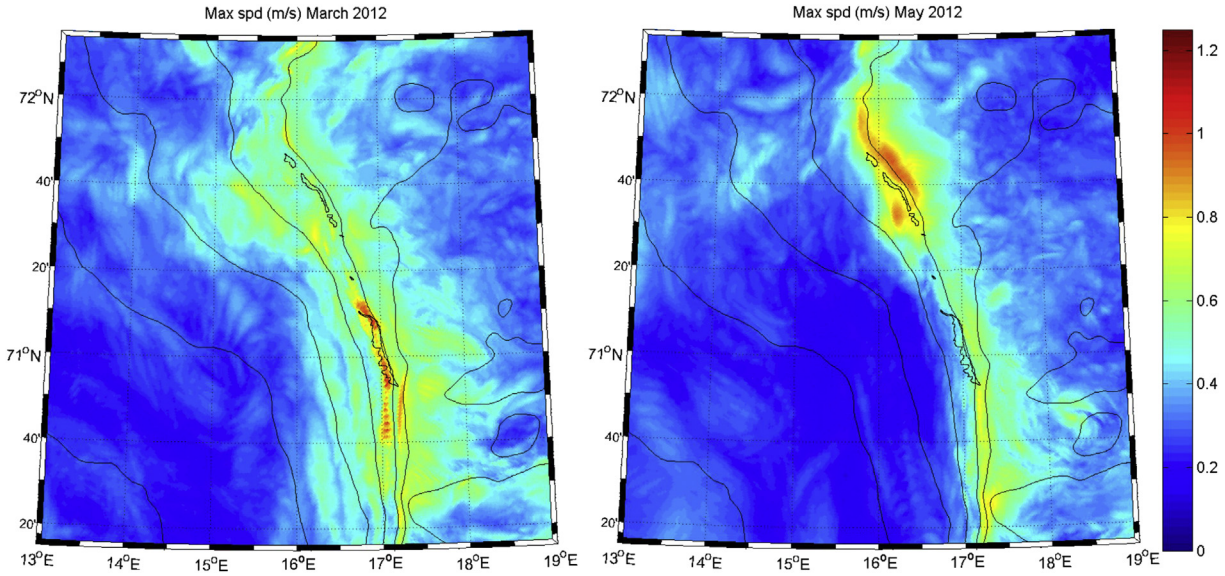

Figure 11. Modelled monthly maximum current speed (m s^{-1}) for March and May 2012 for the deepest model layer, i.e. maximum bottom current speed. Bathymetric contours are drawn for depths 200, 300, 500, 1000, 1500 and 2000 m and the sandwave fields are indicated with black closed contours.

MAREANO videos (www.mareano.no) have also documented sand ripples in gullies with migration direction perpendicular to the depth contours.

6. Oceanography

6.1. Oceanographic measurements

Conductivity, temperature and depth (CTD) data from the survey 28–29 April, 2012 show temperature decreasing with depth, from 6 °C in the upper 400 m to <0 °C below 800 m (Fig. 7). At the deep stations (west of 16°E), the thermocline between NAW and NSAIW was pronounced with a temperature change of 5° from 500 m to c. 800 m in the water column (Fig. 7). More details about the hydrographic measurements are presented in Skarðhamar et al. (in press).

The current measurements from October–December 2010, at 508 m water depth (604 m total water depth), show daily oscillations, with amplitudes reflecting spring-neap variations, and along slope and cross-slope current velocities up to 75 cm s^{-1} and 65 cm s^{-1}, respectively (Fig. 8). The tidal variability was extracted using the Matlab package of Pawlowicz et al. (2002). Based on this, the diurnal periods (K1 and P1) clearly dominate with the major axes of variability in cross-slope direction. In comparison, the strongest semidiurnal component (M2) is an order of magnitude smaller, with more confined uni-directional current in the cross-slope direction. The long periodic components MSF (14 days periodicity) and MM (28 days periodicity) are of similar magnitude as the semidiurnal components, but different in that the uni-directionality is along-slope (Fig. 8). The measurements show relatively equal up- and down-slope magnitudes but stronger northward values in the along-slope velocity. Similar oscillations were present in the measurements from March–April 2012, but with weaker currents: along-slope current velocities up to 60 cm s^{-1}, and cross-slope current velocities up to 40 cm s^{-1} (see Skarðhamar et al., in press for more details). The 2012 measurements show that current velocities 20 m and 60 m above the seabed are approximately similar, and we thus assume that measurements 100 m above the seabed and close to the seabed are comparable.

6.2. Current modelling results

The modelled current field is characterized by a northward contour current, as well as eddies and meanders (Fig. 9). The monthly average current fields show that the contour current is most pronounced in January–March. It largely disintegrates in April when an anticyclone develops near the sandwave fields. The pattern regenerates in September, with strong slope-parallel northerly flow followed by development of large eddies in October, effecting a flow reversal at sandwave field depths. However, embedded in monthly trends are much shorter-term variations with locally high velocities. Snapshots of bottom current fields in May, as an example, when the monthly mean currents are gently following the slope, reveal daily alternating anticyclonic and cyclonic eddies over the slope at the northern sandwave field (Fig. 10).

The monthly maximum bottom current speed (Fig. 11) shows highest values along the slope at the depth of the sandwaves, but is not limited to the sandwave fields. Bottom currents reach velocities of around 1 m s^{-1} in both the northern and southern sandwave fields. Rose plots of modelled bottom currents at selected stations (locations in Fig. 2a, b) are presented in Figure 12. Within the northern sandwave field, the modelled bottom current directions vary with a fan shaped distribution, mainly between west and north. Currents towards west were more pronounced at the up-slope stations compared to the station downslope of the sandwave field, which show more currents towards the north. Bottom current speeds above 40 cm s^{-1} were rare in the southern sandwave field, but were common in the northern sandwave field. The dominating current direction was along slope on all stations in the southern sandwave field, although a fan shaped distribution of the current directions was present also here. Currents towards the southeast are more frequent in the southern than in the northern sandwave area.

7. Sandwave migration from time-lapse multibeam bathymetry

Serial (time-lapse) multibeam datasets across the N2 field are suitable for comparison of the larger sandwaves; each dataset contains noise/artefacts which generally appear as linear

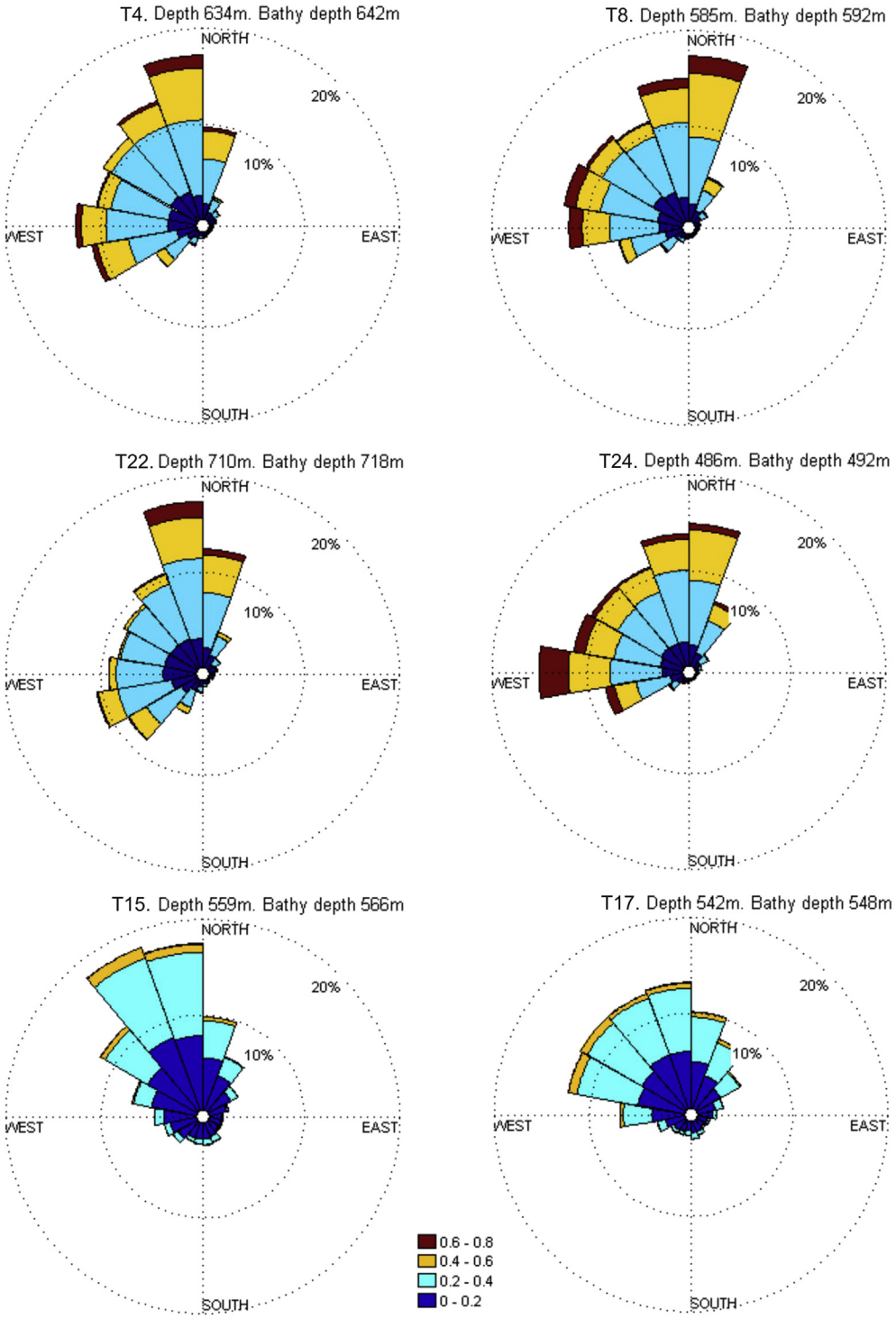

Figure 12. Modelled annual distribution of bottom current direction and speed (m s^{-1}) at the lowest grid cells in positions T4 and T8 in the northern sandwave area, T22 downslope of the northern sandwave area, T24 upslope of the northern sandwave area and in T15 and T17 in the southern sandwave area in 2012. See Figure 2a and b for location of positions.

corrugations in the shaded relief image and reduce capacity to register serial changes in the smaller bedforms. The FFI data offer the most detailed view of the sandwaves and reveal the presence of many smaller sandwaves towards the periphery of the main sandwave fields which were not detected by the MAREANO or UiT surveys. The data quality in S1 is more varied, but again the FFI data reveal the greatest detail, e.g., up to 0.5 m high sandwaves that are obscured by noise in the MAREANO data. The UiT data show more noise than the data from N2.

In addition to serial horizontal differences in bedforms evident in the shaded relief images, vertical differences are frequently 1–3 m – therefore of the same order of magnitude as the sandwaves themselves (only the MAREANO data are corrected for tides). Here, we focus on horizontal comparison of the sandwave datasets. Terrain analysis was performed on each bathymetric dataset to help delineate the sandwave features and quantitative measures of their morphology. Such a methodology has already proven to be useful for the MAREANO data (King et al., 2014). The primary objective

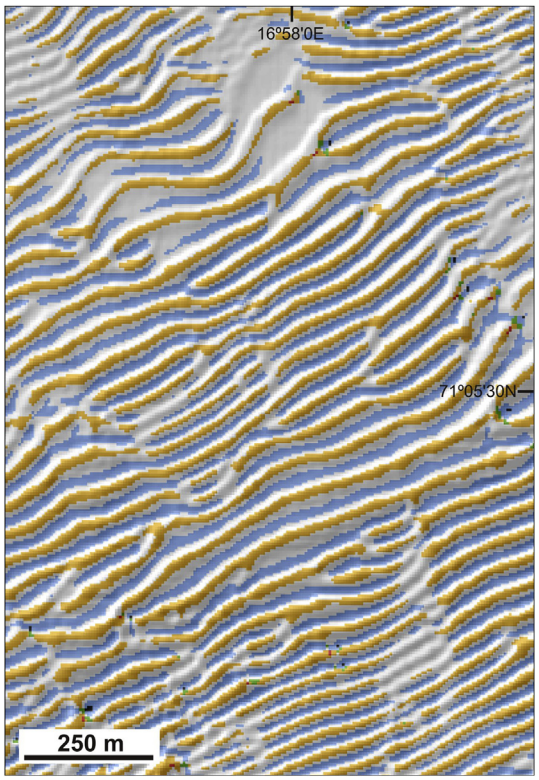

Figure 13. Example of crests (orange) and troughs (blue) identified by automatic feature detection (Wood, 2009) using a 9 × 9 pixel analysis window from the FFI bathymetry dataset with 5 m grid resolution (S1 field). Features are shown draped on shaded relief in order to aid interpretation. (For interpretation of the references to colour in this figure legend, the reader is referred to the web version of this article.)

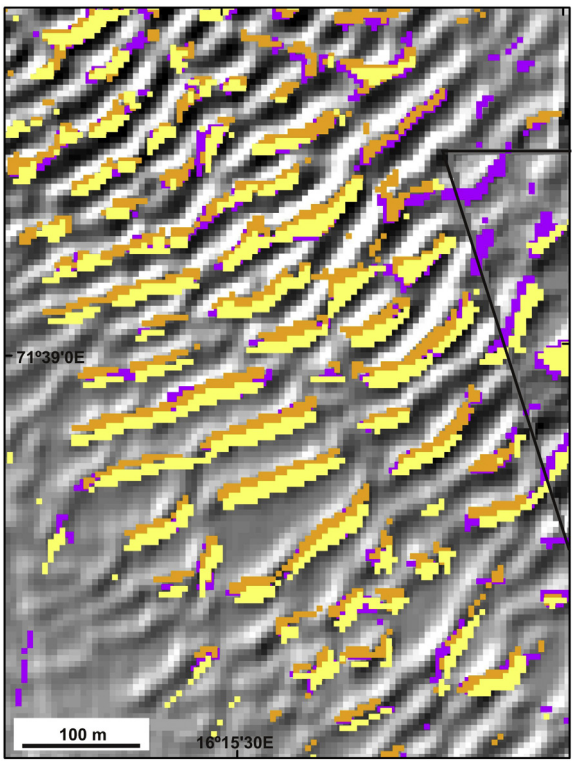

Figure 14. Feature detection example from a part of the N2 sandwave field where migration is most prominent. The figure shows the position of crests identified from three different datasets. Crests from the MAREANO 2008 dataset are shown in yellow. Migration is suggested by the shift in position of these crests when identified from UiT data acquired in June 2012 (purple) and FFI data acquired in November 2012 (orange). No FFI data exist within the black triangle. Features are shown draped on the FFI shaded relief illuminated from the NW. See Figure 15 for location. (For interpretation of the references to colour in this figure legend, the reader is referred to the web version of this article.)

was to compare potential changes in sandwave morphology/position over the time-series datasets.

One method of achieving this is to derive terrain parameters at multiple scales, analysing successively larger-area windows of the seabed. Terrain parameters such as slope, aspect and curvature, are extracted (Wood, 1996; Wilson et al., 2007; Dolan et al., 2012). The feature extraction tools in Landserf v.2.3 software (Wood, 2009) further uses results of terrain analysis to classify terrain into geomorphic feature types (e.g., ridges and channels). Following tests on the MAREANO and FFI data it was decided that a window size of 9 × 9 pixels was appropriate for the present datasets (roughly one-half the original gridding resolution). At this length scale (corresponding to a ground distance of 45 m × 45 m) terrain variables could be analysed and produce results useful for the characterization of sandwaves, yet without undue interference noise from artefacts in the bathymetry data (Bøe et al., 2013).

From feature extraction it is the ridge and channel classes which are most useful in determining the location of sandwave crests and troughs. Using Wood's (1996) definition we "auto-recognize" classes of ridges (sandwave crests, points that lie on a local convexity that is orthogonal to a line with no convexity/concavity) and channels (sandwave troughs, point that lies in a local concavity that is orthogonal to a line with no concavity/convexity). An example of ridge/channel feature classification is shown in Figure 13.

King et al. (2014) used asymmetry measures to infer migration direction. This is a reasonable approach when no time-series data are available for comparison of crest/trough positions. However, now that we have data over a number of years and a robust method for automatic crest/trough detection we selected to use visual analysis of these features across datasets in order to detect possible migration. Due to the limitations of the data (both grid resolution and quality differences) we can only detect changes that are quite large (~>5 m).

For the northern area we compared ridge features (crests) identified in the MAREANO dataset with those identified from the FFI data (Fig. 14). In the southern part of N2 we observe the most prominent migration (Fig. 15). There appears to be a successive NW movement in the position of crests over the years 2008–2012. Some sandwaves appear to have migrated up to 10 m, and we conclude that maximum migration in the range 5–10 m is likely. We noted that small differences in the direction of a profile (used to calculate asymmetry) can yield very different results since the sandwaves are often slightly irregular. The same comparison of crests/troughs was performed in S1 but we were not able to detect appreciable sandwave migration.

8. Discussion

There are very few descriptions of sandwaves on continental slopes. This paper contributes to the understanding of how sandwaves in slope settings (between the continental shelf break and c. 1000 m water depth) form and behave. Such information is important as active sandwaves may cause difficulties for offshore installations. It is also important for understanding benthic species distribution on the slope (e.g., www.mareano.no).

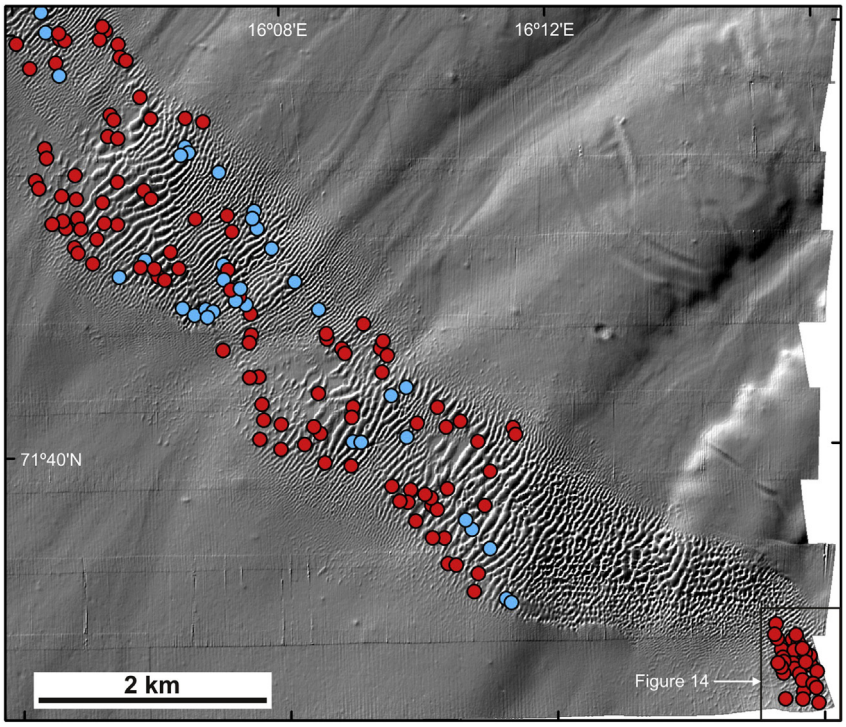

Figure 15. Directions of sandwave migration in the N2 sandwave area determined from changes in crest/trough position between the MAREANO and FFI datasets using automatic feature detection (Wood, 2009). Red dots indicate a crest that has moved NW while blue dots indicate a crest that has moved SE. Dots are shown on shaded relief image (FFI data) illuminated from the NW. The sandwave area in the SE corner is shown in greater detail in Figure 14. For location, see large black rectangle in Figure 2a. (For interpretation of the references to colour in this figure legend, the reader is referred to the web version of this article.)

8.1. Location of sandwave fields in relation to bottom currents

The bottom current in the sandwave area on the Barents Sea continental slope is a product of the northward flowing NAC, which varies in strength throughout the year, and tidally induced topographic waves. Currents measurements in the northern sandwave area show strong current velocity components in cross-slope direction (Fig. 8). Our oceanographic model simulation results show an energetic slope current, with eddies, meanders and topographic waves in the sandwave areas (Fig. 9). The modelled bottom currents generally have components north/north-westwards along the slope, but show strong cross-slope components, forming a fan like distribution of bottom current directions. Figure 11 shows that in May 2012, as an example, the modelled bottom currents were strongest upslope along the shelf break and immediately downslope of the northern fields. Figure 12 shows that, in this area, the majority of bottom currents up-slope of the sandwave fields are directed obliquely downslope towards the west, while bottom currents below the sandwave fields are directed obliquely upslope towards the north. Episodes of currents towards the south occur when eddies interact with the slope. Given that the current speed periodically and regularly exceeds thresholds for medium sand mobility for extended durations, sandwaves can be expected to propagate in all directions over time, although the sector between west and north dominates.

The time-lapse study of bathymetry datasets collected over a 4-year time period shows that these sandwaves migrate. The resolution of the bathymetry data is not high enough to observe small changes but, especially in N2, migration is evident. In the southernmost part of N2 sandwaves may have migrated 5–10 m towards the northwest. In N2, there are also sandwaves migrating towards the south–southeast. This is compatible with earlier inferences based on asymmetry (King et al., 2014) and fits well with the modelling results giving episodes of currents in southerly directions. The downslope bending of the northernmost tip of sandwave field S1 may be caused by local eddies and currents with a predominant downslope component in this area.

Video observations indicate that sand ripples are nearly ubiquitous, superimposed on the sandwaves. Sand ripples also occur between the sandwave fields, but are uncommon in deeper and shallower water. Sand ripples exhibit starkly contrasting directions at the sharp transition from sandwave stoss to lee slopes suggesting local hydraulic regimes which are important to sand transport direction. In this part of the Barents Sea there are no fixed tidal measurement stations, and the directions of the bottom currents at the time of the video observations are thus unknown. However, the tidal variability measured in the northern sandwave field, with the major axes of variability in the cross-slope direction, suggests that ripples migrate along with the tidal current up and down the slope. The direction of migration and sand transport will vary according to the interaction between tidal currents, which sweep around 360° (Figs. 8 and 10), topographic waves and the slope-parallel northward directed contour current. Due to the hydraulic regime close to the seabed, this migration appears to be focussed along sandwave lee slopes and sandwave troughs. There are however variations throughout the year as evidenced by the variation in the strength of the NAC (Fig. 9).

Most sandwave crests are sharp and lee sides steep. All these indications suggest active bedform mobility, both in a mobile layer several centimetres thick and, at a slower pace, in the larger bedforms. The modelled currents with local eddies, cross slope velocities up to 65 cm s^{-1} and daily sand transport up and down the slope fit the observations of current ripples migrating at directions up to 90° relative to the sandwaves. Kenyon (1986) suggested that current greater than 40 cm s^{-1} is needed to form and maintain sandwaves such as those found in this area. Johnson et al. (1982)

and Belderson et al. (1982) have shown that medium grained tidal sands can form large sandwaves on continental shelves when current speeds exceed c. 50 cm s^{-1}.

Bottom current speeds of 60–100 cm s^{-1} (Fig. 11) were modelled in the depth interval where the sandwaves are found, all along the slope and throughout the year but not restricted to sandwave field locations. Thus, our model results help explain why the sandwave fields are found in this 600–800 m depth interval, namely at the transition zone between NAW and NSAIW. The orientation (strike) of the continental slope swings from N–S to NNW–SSE just south of S1. This, in addition to a steeper slope, influences the oceanographic circulation pattern and may explain why sand accumulates in S1 but not farther south.

The present along-slope distribution of sandwave fields apparently results from the location of eddies, meanders and topographic waves, but availability of sand may also be a factor. The monthly maximum bottom current speed (Fig. 11) reveals bands of elevated seabed stress both above and below the northern sandwave field and a similar double band south of the southern field. The northern field example (for May) matches the eddy presence (Fig. 10). This suggests that the sandwave field distribution is partially governed by the relative current strengths surrounding it. Strong currents on its flanks prevent deposition while the eddy components help create a central lower energy zone which is conducive to deposition. A potential implication is that the small, flanking sandwaves are more responsive to short-term change in strength and direction. The lack of observed 3D ripples or sandwaves in the increasing velocity fields is probably related to poor data resolution.

8.2. Sand origin and transport

The sand (Unit 1) in the sandwave fields overlies glacial debris flow deposits (Units 3 and 4) deposited when the ice margin grounded at the shelf break some kilometres up-slope (before c. 15 000 ^{14}C yrs BP). Above the glacial debris, glaciomarine clay with ice rafted material (Unit 2) was deposited when the ice retreated from the shelf and coastal areas. A number of slides (Kenyon, 1987; Vorren et al., 1989; King et al., 2014) occurred afterwards, and stratigraphic relations observed in the TOPAS data suggest that these pre-date sandwave field initiation.

Our grain-size data suggest a possible trend of increasing sorting northwards along the sandwave fields. Although we have too few samples to conclude with any certainty, this is consistent with a sand source from the south and transport towards the north. Also median and mean grain sizes show a decreasing trend in a northerly direction, indicating the same possible transport direction. It is difficult to see a consistent pattern in the rounding of sand grains and petrography.

Seabed sediments outside of the sandwave fields locally have high $CaCO_3$ content, mainly shells, suggesting that benthic animals with shells favour living in the sediments of Units 2–4. Shells are easily eroded and transported in traction because of their large surface/weight ratio and should thus be expected to accumulate in sandwave fields. In the Hola glacial trough outside Vesterålen, medium-coarse-grained bioclastic sand comprises almost 100% of the sand in the large sandwaves accumulated in postglacial times (Bøe et al., 2009), while in Andfjorden, a sand unit with 40–60% $CaCO_3$ content (Hald and Vorren, 1984) occurs unconformably on top of glacigenic sediments. The low $CaCO_3$ content of the sands on the Barents Sea continental slope indicates that shells, being less durable than other minerals, are worn down by intense sand movement within the sandwave fields.

The high quartz content of the sands indicates derivation from older sediments or sedimentary rocks. The nearest outcrops of sedimentary bedrock are far away, along the coast of mainland Norway. Also chert and dolomite suggest erosion of older sediments. Amphibole does not survive deep burial, so high content of this mineral suggests erosion from metamorphic or magmatic rock fragments. Some heavy minerals, i.e. tourmaline, spinel and rutile, are very rare suggesting low content of these in the source area. The obvious source of the sand is the glacigenic sediments on the shelf and slope, which probably contain all components of the sand except for the younger bioclastic components.

Outside the sandwave fields, on the continental slope but also on the continental shelf, a coarse-grained lag on the seabed is almost ubiquitous, while finer-grained sediments occur in depressions and deeper areas (e.g., Hald and Vorren, 1984; Bellec et al., 2009; Bøe et al., 2009). Coarse sediments with cobbles and boulders occur on shallow banks, but also on ridges in deeper water on the shelf. West of Tromsøflaket such ridges, interpreted as

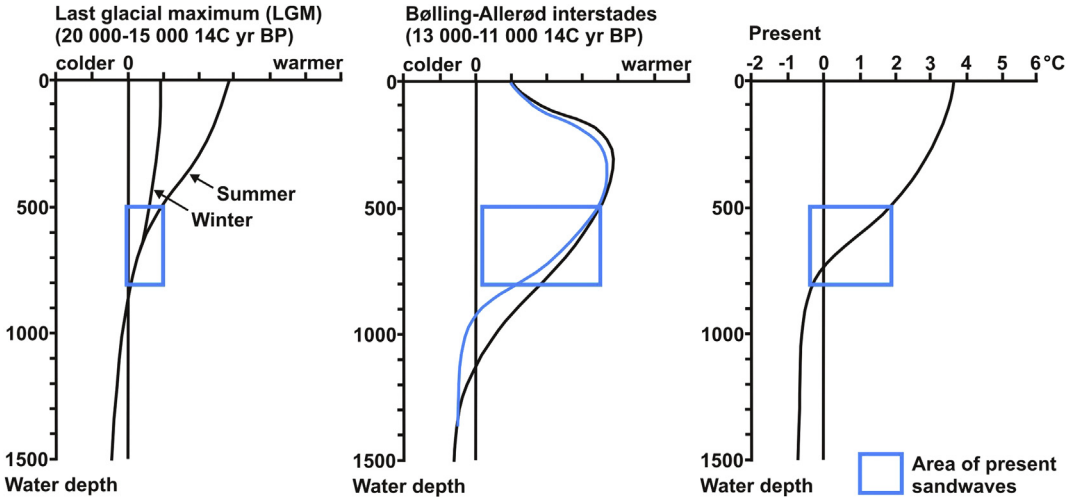

Figure 16. Reconstructed ocean temperature versus water depth along the northwestern Barents Sea margin: (left) LGM (prior to sandwave initiation), (centre) BA interstadial (start of sandwave formation) and at present (right). The vertical scale of the blue boxes marks the depth of present sandwave formation. The horizontal scale indicates the temperature gradients of prevailing water masses. The blue line is an alternative interpretation for the study region based on observation from Rørvik et al. (2013). Note the significantly stronger gradient during the BA compared to the LGM (modified from Rasmussen et al., 2007). (For interpretation of the references to colour in this figure legend, the reader is referred to the web version of this article.)

terminal moraines, occur close to the shelf break. Lag deposit on the slope is commonly developed as layers of mixed sediments a few centimetres thick on top of glacial debris flow and glaciomarine deposits. Hald and Vorren (1984) observed a sharp unconformity between glacigenic sediments and overlying lag deposits/sand.

On the banks along the coast, sea level has risen 50–100 m after the last glaciation. The isostatic rebound contribution to a reduced sea-level rise and the forebulge effect at the banks is not known, thus there is no sea-level curve for these areas. Most of this rise occurred shortly after the ice retreat from the shelf (Rokoengen and Dekko, 1993; Fjalstad and Møller, 1994; Møller, 2000). Much of the glacial bank reworking probably occurred during the sea-level lowstand, when the finest grain fractions (clay, silt, sand) were washed off banks and shallow areas by wave action. This may be similar to the situation in the Celtic Sea, where erosion and sand bank growth has been interpreted to have occurred during times of lower sea level during the early deglacial (Berné et al., 1998). It is possible that sand eroded from the outer parts of the banks off Troms (e.g., Malangsgrunnen, Fig. 1) was transported offshore by waves and currents and thereafter along the continental slope towards the sandwave fields. The western parts of Tromsøflaket were probably less eroded during the sea level low stand because of greater water depths.

The bottom current modelling results (Fig. 12) indicate ongoing, net transport of sand into the sandwave fields. Bottom currents are generally towards the northwest and west-northwest, but a more detailed study of the rose diagrams developed for different localities shows a clear pattern. In N1 (Fig. 2a), currents are generally towards the northwest, indicating sand transport in that direction. In N2 there is more variation in current direction and strength. Currents towards the northwest are common, but the strongest and most frequent currents are towards the north and west. Stations in shallower water, closer to the shelf break have their strongest currents directed towards the west, obliquely downslope towards N2. The modelled bottom current speeds and velocity vectors for one tidal cycle in mid May (Fig. 10), as an example, show strong variation in bottom current direction and current velocity on Tromsøflaket. During parts of the tidal cycle, currents are directed westward and are strong enough to erode and transport fine-medium-grained sand towards the shelf break and further downslope. Some of the sand may thus originate from the glacial deposits on Tromsøflaket.

The modelling results show that bottom currents stronger than c. 70 cm s^{-1} occur down to 1000 m depth. Such current strength is sufficient to erode particles up to 3 mm diameter and to transport larger pebbles (Hjulstrøm, 1935; Johnson et al., 1982). Lag deposits lower on the slope (Fig. 2a, b) testify that the seabed has been eroded by bottom currents. The modelling station downslope of N2 (T22, Figs. 2a and 12) has its strongest currents directed towards the north, obliquely upslope towards N2. It is thus likely that sand from lower on the slope is transported upslope to accumulate in the sandwave fields. Cyclonic and anticyclonic vortexes occur daily during the tidal cycle, and vortices traverse the slope throughout the year. Further these strong cross-slope velocities likely induce energetic high-frequency internal wave packets at the main pycnocline focused where it intercepts the bottom (see also Padman et al., 1992). These features clearly causes changing sediment transport directions but the net vectors and effects remain unclear. King et al. (2014) found sandwave morphological anomalies related to the gullies and we now have established ample sand transport potential both up- and down-slope. The gullies, often with a funnel shape, are a likely conduit for enhanced sand transport. The lower slope contour current winnowing conceivably moves sand into the gullies while other mechanisms (eddies and topographic waves) further transport it up and down these pathways and into the relatively stable sandwave fields.

Within and upslope of S1, the rose diagrams (Fig. 12) show that currents up to 40 cm s^{-1} may be directed in almost any direction, but the strongest currents (40–60 cm s^{-1}) are along the slope towards the north–northwest. This suggests that sand may be derived from both lower and higher on the slope also in S1, but to a lesser degree than in the northern sandwave fields. Sand in S1 may to a large degree be derived from farther south on the slope. Erosion of the seabed may possibly take place down to 1000 m depth.

The sand unit is not a simple contourite (e.g., Lowell and Stow, 1981) deposited by NAW flowing steadily along the continental slope. Instead, the location of individual sandwave fields, both laterally and perpendicular to the slope, is strongly influenced by eddies and topographic waves. The sandwave fields can be described as a kind of “plastered contourite” in the classification of Faugères et al. (1993).

8.3. Age of the sandwave fields

The currents in the slope region are due to two mechanisms; 1) the northward partly baroclinic flow due to the density (temperature) contrast between NAW and deep water, and 2) prominent continental shelf waves due to resonant interaction with the diurnal tides. The prior component is likely to change during different palaeo-climate states, whereas the latter was likely a factor also during the glacial periods. Changing stratification during glacial–interglacial periods changes the properties of the small-scale internal waves in the slope region.

The inception of the sandwaves is regarded as post-glacial as they transect slide scars of late glacial/postglacial age, as well as the uppermost glacial debris flow and glaciomarine deposits (King et al., 2014). Prior to the Bølling–Allerød (BA) interstadial (~13 000–11 000 ^{14}C yr BP), cold NAW (>2–4 °C) was present along the northwestern Barents Sea margin (during the late glacial maximum, LGM) down to a depth of at least 1500 m (Rasmussen et al., 2007). This corroborates observations from the Arctic–Atlantic gateway region where presence of Atlantic water is inferred down to at least 1000 m during the LGM (e.g., Knies et al., 1999; Nørgaard Pedersen et al., 2003). For the Lofoten margin, Rørvik et al. (2013) found evidence for a strong along-slope advection of NAW during the LGM as well. High Δ^{13}C values of benthic foraminifera, however, indicate the predominance of well-ventilated Glacial North Atlantic Intermediate Water (i.e. analogous to NSAIW) at ~1100 m water depth during the LGM (Rørvik et al., 2013; Rasmussen and Thomsen, 2009; Oppo and Lehman, 1993).

According to Rasmussen et al. (2007), the LGM temperature gradient between the subsurface and the bottom waters at 1500 m along the northwestern Barents Sea margin was relatively low compared to today (<3 °C). Hence, the bottom currents of this homogenous water mass were probably not strong enough to create large scale sandwaves, most likely due to weaker temperature/salinity gradients between the two prevailing water masses (NAW/NSAIW). This overall pattern did not change during course of the initial deglaciation (15 000–13 000 ^{14}C yr BP). Due to development of a strong halocline induced by cold melt water from retreating ice sheets, the Atlantic water entered the deeper waters down to at least 1000 m water depth (Rasmussen et al., 2007; Rasmussen and Thomsen, 2009).

An oceanographic pattern like today, but with still prevailing cold surface waters due to meltwater discharge, is first observed during the BA interstadial (<13 000 ^{14}C yr BP) (e.g., Bauch et al., 2001; Rasmussen et al., 2002, 2007; Slubowska-Woldengren et al., 2007; Meland et al., 2008). Koç et al. (1993) showed that NAW appeared at the surface in the southern Norwegian Sea between 13 400 and 13 000 ^{14}C yr BP. Sarnthein et al. (2003) stated that the present Holocene-style circulation mode persisted over the

last 12 800 ^{14}C yr BP and that glacial to interglacial differences in the evolution of wave crests and troughs (further south, in the mid-Atlantic region) may indicate intermittent accreting sediment regimes (Sarnthein and Mienert, 1986). Moreover, a number of studies have shown that open-ocean convection and meridional overturning in the Nordic seas strengthened during the BA interstadial. Meland et al. (2008) concluded from benthic isotope records that convected water entrained shallower depths than today, however, had similar properties as today at intermediate depths. This observation corroborates findings from the northwestern Barents Sea margin, where stronger temperature gradients between subsurface and bottom waters are reported during the BA interstadial (Fig. 16).

An age of 11 000–13 000 ^{14}C yrs BP for the onset of sand accumulation in the sandwave fields agrees thus very well with the establishment of a modern oceanographic circulation pattern in the Nordic Sea including deep water convection and strong boundary conditions (strong gradients) between NAW and NSAIW at 500–800 m water depth in the study area (Fig. 16). It is however possible that the sandwave field formation is younger than the onset of sand accumulation on the slope.

9. Conclusions

Sandwaves on the southwestern Barents Sea continental margin are found in c. 475–800 m water depth. They occur in several clearly defined sandwave fields in a northern area (sandwave fields N1–N6) and a southern area (sandwave field S1). The sandwave fields cover 130 km^2 of the continental slope, while total sand volume approximates 72 $\times$ 10^6 m^3. The largest sandwaves occur in sandwave fields N2 and S1, where they reach heights of 6 m from trough to crest. Maximum and average wavelengths are 205 m and 64 m, respectively. The majority of the sandwaves are sinusoidal with asymmetric stoss–lee relationships. The sand is well sorted, medium grained and with subangular to subrounded sand grains. Quartz is the dominating mineral, but the sand contains a large variety of minerals, rock fragments and biogenic components.

Ocean current modelling results suggest that the sandwave fields are in equilibrium with present-day hydrodynamics. There is probably a gradual northward movement of sand by the Norwegian Atlantic Current, but this movement is counteracted by currents in other directions that occur daily during the tidal cycle and regularly throughout the year. One vortex appears to occur daily in a stable position at the northern sandwave area, while other vortices move along the slope and cause bottom currents in various directions, both up and down the slope as well as in southerly and easterly directions. Time-lapse multibeam bathymetry analysis shows that within small domains of N2, sandwaves have migrated 5–10 m towards the northwest over a 4 year period while in other domains they have moved towards the southeast.

Oceanographic measurements show daily oscillations and clear spring-neap variations of current speed and directions in the northern sandwave field, and along-slope and cross-slope current velocities up to 75 cm s^{-1} and 65 cm s^{-1}, respectively. Modelled current velocities are high and reach 75–100 cm s^{-1}, both within the sandwave fields, lower on the slope and higher on the slope. The various currents cause sandwave formation and extensive sand movement within the sandwave fields and towards the sandwave fields. The combined effect of the along slope Norwegian Atlantic Current, tidal period topographic waves, eddies and sand supply causes the sand to accumulate in distinct sandwave fields along the boundary between North Atlantic Water and Norwegian Sea Intermediate Water.

The modelled variable bottom current fields (speed and direction) suggest that the sand may have originated from the upper part of the continental slope, but also from the adjacent shelf, from lower on the slope and from south of the sandwave fields. The sand mainly originates from glacial debris flow/glaciomarine deposits on the slope and from till on the shelf, but some is of more recent, biogenic origin. A coarse-grained lag remains on the seabed where current erosion has removed fine-grained sediments and transported sand into the sandwave fields. Sand accumulation in the sandwave fields may have started soon after the present ocean circulation pattern was established, 11 000–13 000 ^{14}C yrs BP.

Acknowledgements

This research was supported by MAREANO (www.mareano.no) and the Norwegian Deepwater Programme (NDP). The numerical model computations were performed at the Norwegian Supercomputer facilities (www.notur.no). We thank the captain and crew on RV G.O. Sars, RV Johan Hjort and RV Helmer Hanssen for cooperation on several cruises and the Norwegian coast guard that recovered one of our moorings adrift in sea. Two anonymous reviewers are thanked for constructive comments to the manuscript.

References

Albretsen, J., Sperrevik, A.K., Staalstrøm, A., Sandvik, A.D., Vikebø, F., Asplin, L., 2011. NorKyst-800 Report No. 1: User Manual and Technical Descriptions. Fisken og havet, 2. Institute of Marine Research.

Andreassen, K., Nilsen, L.C., Rafaelsen, L.C., Kuilman, B.R.L., 2004. Three-dimensional seismic data from the Barents Sea margin reveal evidence of past ice streams and their dynamics. Geology 32 (8), 729–732.

Baraza, J., Ercilla, G., Nelson, C.H., 1999. Potential geological hazards on the eastern Gulf of Cadiz slope (SW Spain). Mar. Geol. 155, 191–215.

Bauch, H.A., Erlenkeuser, H., Spielhagen, R.F., Struck, U., Matthiessen, J., Thiede, J., Heinemeier, J., 2001. A multiproxy reconstruction of the evolution of deep and surface waters in the subarctic Nordic seas over the last 30.000 years. Quat. Sci. Rev. 20, 659–678.

Belderson, R.H., Johnson, M.A., Kenyon, N.H., 1982. Bedforms. In: Stride, A.H. (Ed.), Offshore Tidal Sands: Processes and Deposits. Chapman & Hall, London, pp. 27–57.

Beldring, S., Engeland, K., Roald, L.A., Sælthun, N.R., Voksø, A., 2003. Estimation of parameters in a distributed precipitation-runoff model for Norway. Hydrol. Earth Syst. Sci. 7, 304–316.

Bellec, V.K., Dolan, M.F.J., Bøe, R., Thorsnes, T., Rise, L., Buhl-Mortensen, L., Buhl-Mortensen, P., 2009. Sediment distribution and seabed processes in the Troms II area - offshore North Norway. Nor. J. Geol. 89, 29–40.

Berné, S., Marsset, T., Lericolais, T., Bourillet, J.-F., De Batist, M., 1998. Erosional offshore sand ridges and lowstand shore faces: examples from the tide and wave dominated environments around France. J. Sediment. Res. 68, 540–555.

Blindheim, J., 1990. Arctic intermediate water in the Norwegian sea. Deep-Sea Res. A Oceanogr. Res. Pap. 37 (9), 1475–1489.

Bøe, R., Bellec, V.K., Dolan, M.F.J., Buhl-Mortensen, P.B., Buhl-Mortensen, L., Rise, L., 2009. Giant sand waves in the Hola glacial trough off Vesterålen, North Norway. Mar. Geol. 267, 36–54.

Bøe, R., Winsborrow, M., Rise, L., Dolan, M., Chand, S., Knies, J., Walderhaug, O., Bellec, V., 2013. Sandwaves and Sand Transport on the Barents Sea Continental Margin. NGU Report 2013.005, 85 pp. Geological Survey of Norway. http://www.ngu.no/upload/Publikasjoner/Rapporter/2013/2013_005.pdf.

Buhl-Mortensen, P.B., Buhl-Mortensen, L., Dolan, M., Dannheim, J., Kröger, K., 2009. Megafaunal diversity associated with marine landscapes of northern Norway: a preliminary assessment. Nor. J. Geol. 89, 163–171.

Dolan, M.F.J., 2012. Calculation of Slope Angle from Bathymetry Data Using GIS - Effects of Computation Algorithms, Data Resolution and Analysis Scale. NGU Report 2012.041, 44 pp. Geological Survey of Norway. http://www.ngu.no/upload/Publikasjoner/Rapporter/2012/2012_041.pdf.

ERA-interim, 2014. http://www.ecmwf.int/research/era/do/get/era-interim.

Faugères, J.C., Mézerais, M.L., Stow, D.A.V., 1993. Contourite drift types and their distribution in the North and South Atlantic Ocean basins. Sediment. Geol. 82, 189–203.

Faugères, J.C., Stow, D.A.V., Imbert, P., Viana, A., 1999. Seismic features diagnostic of contourite drifts. Mar. Geol. 162, 1–38.

Fjalstad, A., Møller, J.J., 1994. Submerged and tilted coastal features off Troms, northern Norway: a reply. Nor. Geol. Tidsskr. 74, 241–244.

Flemming, B.W., 1980. Sand transport and bedform patterns on the continental shelf between Durban and Port Elizabeth (southeast African continental margin). Sediment. Geol. 26, 179–205.

Folk, R.L., Ward, W.C., 1957. Brazos River bar: a study in the significance of grain size parameters. J. Sediment. Petrol. 37, 3–26.

Furevik, T., 1998. On the Atlantic Inflow in the Nordic Seas: Bifurcation and Variability (Dr. Scient. thesis). University of Bergen, Bergen.

Furevik, T., 2001. Annual and interannual variability of Atlantic Water temperatures in the Norwegian and Barents Seas: 1980-1996. Deep-Sea Res. I 48 (2), 383–404.
Gascard, J.-C., Mork, K.A., 2008. Climatic importance of large-scale and mesoscale circulation in the Lofoten Basin deduced from Lagrangian observations. In: Dickson, R.R., et al. (Eds.), Arctic-Subarctic Ocean Fluxes. Springer Science, pp. 131–143.
Habgood, E.L., Kenyon, N.H., Masson, D.G., Akhmetzhanov, A., Weaver, P.P.E., Gardner, J., Mulder, T., 2003. Deep-water sediment wave fields, bottom current sand channels and gravity flow channel-lobe systems: Gulf of Cadiz, NE Atlantic. Sedimentology 50, 483–510.
Haidvogel, D.B., Arango, H.G., Budgell, W.P., Cornuelle, B.D., Curchitser, E., Di Lorenzo, E., Fennel, K., Geyer, W.R., Hermann, A.J., Lanerolle, L., Levin, J., McWilliams, J.C., Miller, A.J., Moore, A.M., Powell, T.M., Shchepetkin, A.F., Sherwood, C.R., Signell, R.P., Warner, J.C., Wilkin, J., 2008. Ocean forecasting in terrain-following coordinates: formulation and skill assessment of the Regional Ocean Modeling System. J. Comput. Phys. 227 (7), 3595–3624.
Hald, M., Vorren, T.O., 1984. Modern and Holocene foraminifera and sediments on the continental shelf off Troms, North Norway. Boreas 13, 133–154.
Hanquiez, V., Mulder, T., Lecroart, P., Gonthier, E., Marchès, E., Voisset, M., 2007. High resolution seafloor images in the Gulf of Cadiz, Iberian margin. Mar. Geol. 246, 42–59.
Hansen, B., Østerhus, S., 2000. North Atlantic–Nordic seas exchanges. Prog. Oceanogr. 45 (2), 109–208.
Haugan, P.M., Evensen, G., Johannessen, J.A., Johannessen, O.M., Pettersson, L.H., 1991. Modeled and observed mesoscale circulation and wave-current refraction during the 1988 Norwegian continental shelf experiment. J. Geophys. Res. Oceans 96 (C6), 10487–10506.
Heathershaw, A.D., Hall, P., Huthnance, J.M., 1998. Measurements of the slope current, tidal characteristics and variability west of Vestfjorden, Norway. Cont. Shelf Res. 18 (12), 1419–1453.
Heezen, B.C., Hollister, C.D., 1971. The Face of the Deep. Oxford University Press, New York, pp. 384–389.
Hjulstrøm, F., 1935. The morphological activity of rivers as illustrated by river Fyris. Bull. Geol. Inst. Upps. 25, 89–122.
Hopkins, T.S., 1991. The Gin sea - a synthesis of its physical oceanography and literature-review 1972-1985. Earth Sci. Rev. 30 (3–4), 175–318.
Johnson, M.A., Kenyon, N.H., Belderson, R.H., Stride, A.H., 1982. Sand transport. In: Stride, A.H. (Ed.), Offshore Tidal Sands: Processes and Deposits. Chapman & Hall, London, pp. 58–94.
Kenyon, N.H., 1986. Evidence from bedforms for a strong poleward current along the upper continental slope of northwest Europe. Mar. Geol. 72, 186–198.
Kenyon, N.H., 1987. Mass-wasting features on the continental slope of northwest Europe. Mar. Geol. 74, 57–77.
Kenyon, N.H., Belderson, R.H., 1973. Bedforms of the Mediterranean undercurrent observed with sidescan sonar. Sediment. Geol. 9, 77–99.
King, E.L., Bøe, R., Bellec, V.K., Rise, L., Skarðhamar, J., Ferré, B., Dolan, M., 2014. Contour current driven continental slope-situated sandwaves with effects from secondary current processes on the Barents Sea margin offshore Norway. Mar. Geol. 353, 108–127.
Knies, J., Vogt, C., Stein, R., 1999. Late Quaternary growth and decay of the Svalbard/Barents Sea ice sheet and paleoceanographic evolution in the adjacent Arctic Ocean. Geo-Mar. Lett. 18, 195–202.
Koç, N., Jansen, E., Haflidason, H., 1993. Paleoceanographic reconstructions of surface ocean conditions in the Greenland, Iceland and Norwegian Seas through the last 14 ka based on diatoms. Quat. Sci. Rev. 12, 115–140.
Laberg, J.S., Vorren, T., 1995. Late Weichselian submarine debris flow deposits on the Bear Island Trough Mouth Fan. Mar. Geol. 127, 45–72.
Laberg, J.S., Andreassen, K., Knies, J., Vorren, T.O., Winsborrow, M., 2010. Late Pliocene-Pleistocene development of the Barents Sea Ice Sheet. Geology 38 (2), 107–110.
Landvik, J.Y., Bondevik, S., Elverhøi, A., Fjeldskaar, W., Mangerud, J., Salvigsen, O., Siegert, M.J., Svendsen, J.I., Vorren, T.O., 1998. The last glacial maximum of Svalbard and the Barents Sea area: ice sheet extent and configuration. Quat. Sci. Rev. 17 (1–3), 43–75.
Lowell, J.P.B., Stow, D.A.W., 1981. Identification of ancient sandy contourites. Geology 9, 347–349.
Mangerud, J., Gulliksen, S., 1975. Apparent radiocarbon ages of recent marine shells from Norway, Spitsbergen, and Arctic Canada. Quat. Res. 5, 263–273.
Masson, D.G., 2001. Sedimentary processes shaping the eastern slope of the Faeroe-Shetland Channel. Cont. Shelf Res. 21, 825–857.
Meland, M.Y., Dokken, T.M., Jansen, E., Hevrøy, K., 2008. Water mass properties and exchange between the Nordic seas and the northern North Atlantic during the period 23-6 ka: benthic oxygen isotopic evidence. Paleoceanography 23, PA1210. http://dx.doi.org/10.1029/2007PA001416.
MET, 2014. http://thredds.met.no.
Møller, J.J., 2000. Submerged littoral sediments, beach ridges and wave-cut platforms off Troms, North Norway: revisiting old questions. Nor. Geol. Tidsskr. 80, 203–212.
Mork, K.A., Skagseth, Ø., 2010. A quantitative description of the Norwegian Atlantic Current by combining altimetry and hydrography. Ocean Sci. 6, 901–911.
NDP, 2014. http://www.epim.no/norwegian-deepwater-programme.
Nørgaard-Pedersen, N., Spielhagen, R.F., Erlenkeuser, H., Grootes, P.M., Heinemeier, J., Knies, J., 2003. Arctic Ocean during the last glacial maximum: Atlantic and polar domains of surface water mass distribution and ice cover. Paleoceanography 18, 1063. http://dx.doi.org/10.1029/2002PA000781.
Oppo, D.W., Lehman, S.J., 1993. Mid-depth circulation of the subpolar North Atlantic during the last glacial maximum. Science 259, 1148–1152.
Ottesen, D., Stokes, C.R., Rise, L., Olsen, L., 2008. Ice-sheet dynamics and ice streaming along the coastal parts of northern Norway. Quat. Sci. Rev. 27 (9–10), 922–940.
Padman, L., Plueddemann, A.J., Muench, R.D., Pinkel, R., 1992. Diurnal tides near the Yermak Plateu. J. Geophys. Res. 97 (C8), 12639–12652.
Pawlowicz, R., Beardsley, B., Lentz, S., 2002. Classical tidal harmonic analysis including error estimates in MATLAB using T_TIDE. Comput. Geosci. 28, 929–937.
Poulain, P.M., WarnVarnas, A., Niiler, P.P., 1996. Near-surface circulation of the Nordic seas as measured by Lagrangian drifters. J. Geophys. Res. Oceans 101 (C8), 18237–18258.
Rafaelsen, B., Andreassen, K., Kuilman, L.W., Lebesbye, E., Hogstad, K., Midtbø, M., 2002. Geomorphology of buried glacigenic horizons in the Barents Sea from three dimensional seismic data. In: Dowdeswell, J.A., Ó Cofaigh, C. (Eds.), Glacier-influenced Sedimentation on High-latitude Continental Margins, Geological Society of London, Special Publication, vol. 203, pp. 259–276.
Rasmussen, T.L., Thomsen, E., 2009. Ventilation changes in intermediate water on millennial time scales in the SE Nordic seas, 65–14 kyr BP. Geophys. Res. Lett. 36, L01601. http://dx.doi.org/10.1029/2008GL036563.
Rasmussen, T.L., Bäckström, D., Heinemeier, J., Klitgaard-Kristensen, D., Knutz, P.C., Kuijpers, A., Lassen, S., Thomsen, E., Troelstra, S.R., van Weering, T.C.E., 2002. The Faroe-Shetland Gateway: Late Quaternary water mass exchange between the Nordic seas and the northeastern Atlantic. Mar. Geol. 188, 165–192.
Rasmussen, T.L., Thomsen, E., Slubowska, M.A., Jessen, S., Solheim, A., Koç, N., 2007. Paleoceanographic evolution of the SW Svalbard margin (76°N) since 20,000 14C yr BP. Quat. Res. 67, 100–114.
Reeder, D.B., Ma, B.B., Yang, Y.J., 2011. Very large subaqueous sand dunes on the upper continental slope in the South China Sea generated by episodic, shoaling deep-water internal solitary waves. Mar. Geol. 279, 12–18.
Rise, L., Chand, S., Haflidason, H., L'Heureux, J.-S., Hjelstuen, B.O., Bellec, V., Longva, O., Brendryen, J., Vanneste, M., Bøe, R., 2012. Investigations of slides at the upper continental slope off Vesterålen, North Norway. In: Yamada, Y., et al. (Eds.), Submarine Mass Movements and Their Consequences (5th International Symposium). Springer, pp. 167–176.
Rokoengen, K., Dekko, T., 1993. Submerged and tilted coastal features off Troms, northern Norway. Nor. Geol. Tidsskr. 73, 198–208.
Rørvik, K.-L., Rasmussen, T.L., Hald, M., Husum, K., 2013. Intermediate water ventilation in the Nordic seas during MIS 2. Geophys. Res. Lett. 40, 1805–1810.
Rüther, D.C., Mattingsdal, R., Andreassen, K., Forwick, M., Husum, K., 2011. Seismic architecture and sedimentology of a major grounding zone system deposited by the Bjørnøyrenna Ice Stream during Late Weichselian deglaciation. Quat. Sci. Rev. 30, 2776–2792.
Sarnthein, M., Mienert, J., 1986. Sediment waves in the eastern equatorial Atlantic: sediment record during Late Glacial and Interglacial times. In: Summerhayes, C.P., Shackleton, N.J. (Eds.), 1986, North Atlantic Palaeoceanography, Geological Society Special Publ. No, vol. 21, pp. 119–130.
Sarnthein, M., Van Kreveld, S., Erlenkeuser, H., Grootes, P.M., Kucera, M., Pflaumann, U., Schulz, M., 2003. Centennial-to-millennial scale periodicities of Holocene climate and sediment injections off the western Barents Sea shelf, 75°N. Boreas 32, 447–461.
Shchepetkin, A.F., McWilliams, J.C., 2005. The Regional Ocean Modeling System (ROMS): a split-explicit, free-surface, topography following coordinate oceanic model. Ocean Model. 9, 347–404.
Skarðhamar, J., Skagseth, Ø., Albretsen, J., 2014. Diurnal tides on the Barents Sea continental margin. Deep-Sea Res. (in press).
Slubowska-Woldengren, M., Rasmussen, T.L., Koç, N., Klitgaard-Kristensen, D., Nilsen, F., Solheim, A., 2007. Advection of Atlantic water to the western and northern Svalbard shelf since 17,500 cal yr BP. Quat. Sci. Rev. 26, 463–478.
Sættem, J., Poole, D.A.R., Ellingsen, L., Sejrup, H.P., 1992. Glacial geology of outer Bjørnøyrenna, southwestern Barents Sea. Mar. Geol. 103, 15–51.
Sættem, J., Bugge, T., Fanavoll, S., Goll, R.M., Mørk, A., Mørk, M.B.E., Smelror, M., Verdenius, J.G., 1994. Cenozoic margin development and erosion of the Barents Sea: core evidence from southwest of Bjørnøya. Mar. Geol. 118, 257–281.
Viana, A.R., Faugères, J.-C., Stow, D.A.W., 1998. Bottom-current-controlled sand deposits - a review of modern shallow- to deep-water environments. Sediment. Geol. 115, 53–80.
Vorren, T.O., Kristoffersen, Y., 1986. Late Quaternary glaciation in the south-western Barents Sea. Boreas 15, 51–59.
Vorren, T.O., Laberg, J.S., 1996. Late glacial air temperature, oceanography and ice sheet interactions in the southern Barents Sea region. In: Andrews, J.T., et al. (Eds.), Late Quaternary Palaeoceanography of the North Atlantic Margins, Geological Society of London, Special Publication, vol. 111, pp. 303–321.
Vorren, T.O., Lebesbye, E., Andreassen, K., Larsen, K.B., 1989. Glacigenic sediments on a passive continental margin as exemplified by the Barents Sea. Mar. Geol. 85, 251–272.
Vorren, T.O., Richardsen, G., Knutsen, S.-M., Henriksen, E., 1991. Cenozoic erosion and sedimentation in the western Barents Sea. Mar. Pet. Geol. 8, 317–340.
Vorren, T.O., Laberg, J.S., Blaume, F., Dowdeswell, J.A., Kenyon, N.H., Mienert, J., Rumohr, J., Werner, F., 1998. The Norwegian-Greenland Sea continental margins: morphology and late Quaternary sedimentary processes and environment. Quat. Sci. Rev. 17, 273–302.

Wilson, M.F.J., O'Connell, B., Brown, C., Guinan, J.C., Grehan, A.J., 2007. Multi-scale terrain analysis of multibeam bathymetry data for habitat mapping on the continental slope. Mar. Geod. 30 (1–2), 3–35.
Winsborrow, M.C.M., Andreassen, K., Corner, G.D., Laberg, J.S., 2010. Deglaciation of a marine-based ice sheet: Late Weichselian palaeo-ice dynamics and retreat in the southern Barents Sea reconstructed from onshore and offshore glacial geomorphology. Quat. Sci. Rev. 29, 424–442.
Wood, J., 1996. The Geomorphological Characterisation of Digital Elevation Models (Ph.D. thesis). University of Leicester, 185 pp.
Wood, J., 2009. Landserf Version 2.3. www.landserf.org.
Wynn, R.B., Stow, D.A.V., 2002. Classification and characterization of deep-water sediment waves. Mar. Geol. 192, 7–22.
www.mareano.no.